A high-order accurate five-equations compressible multiphase approach for viscoelastic fluids and solids with relaxation and elasticity

Mauro Rodriguez *, Eric Johnsen

Department of Mechanical Engineering, University of Michigan, Ann Arbor, MI 48109, USA

ARTICLE INFO

ABSTRACT

A novel Eulerian approach is proposed for numerical simulations of wave propagation in viscoelastic media, for application to shocks interacting with interfaces between fluids and solids. We extend the five-equations multiphase interface-capturing model, based on the idea that all the materials (gases, liquids, solids) obey the same equation of state with spatially varying properties, to incorporate the desired constitutive relation; in this context, interfaces are represented by discontinuities in material properties. We consider problems in which the deformations are small, such that the substances can be described by linear constitutive relations, specifically, Maxwell, Kelvin–Voigt or generalized Zener models. The main challenge lies in representing the combination of viscoelastic, multiphase and compressible flow. One particular difficulty is the calculation of strains in an Eulerian framework, which we address by using a conventional hypoelastic model in which an objective time derivative (Lie derivative) of the constitutive relation is taken to evolve strain rates instead. The resulting eigensystem is analyzed to identify wave speeds and characteristic variables. The spatial scheme is based on a solution-adaptive formulation, in which a discontinuity sensor discriminates between smooth and discontinuous regions. To compute the convective fluxes, explicit high-order central differences are applied in smooth regions, while a high-order finite-difference Weighted Essentially Non-Oscillatory (WENO) scheme is used at discontinuities (shocks, material interfaces and contacts). The numerical method is verified in a comprehensive fashion using a series of smooth and discontinuous (shocks and interfaces), one- and two-dimensional test problems.

© 2018 Elsevier Inc. All rights reserved.

1. Introduction

Recent years have seen the emergence of the need for simulating shock and other high-frequency-content waves (e.g., blasts, therapeutic ultrasound pulses, shocks emitted by collapsing bubbles) interacting with solid objects whose stiffnesses can range from soft (e.g., human tissue) [83] to moderate (e.g., elastomeric coatings in naval propulsors) [64,8] to hard (metals or concrete) [17,58,49]. An example of interest is the impingement of a shock propagating in a liquid upon a solid object and its subsequent propagation in the solid, which presents the computational challenge of accurately and robustly representing compressible, multi-material flows with shocks, shear waves, and viscoelastic deformations of the solid. High-order

---

* Corresponding author.
  E-mail addresses: mrdz@umich.edu (M. Rodriguez), ejohnsen@umich.edu (E. Johnsen).

accurate shock- and interface-capturing schemes have emerged as viable approaches for shocks in multi-material flows, for instance, to simulate gas bubbles collapsing in water near solid objects and the shock waves thereby produced [36,72,76, 16]. Given their high order of accuracy, these approaches accurately represent high-frequency-content waves emitted by bubble collapse. However, an accurate description of the solid mechanics is challenging. Two main strategies have been pursued: coupling the flow solver with a solid mechanics solver (e.g., arbitrary Lagrangian–Eulerian or ALE approaches), or solving the fluid and solid mechanics in a single framework. The former has been used for multi-component fluid-structure interaction problems such as shock-bubble interaction near a solid object [85] and for flows with shocks using the Ghost Fluid method [6,66,29]. However, the extreme fluid distortions and vorticity generated in problems of interest (e.g., bubble collapsing near an elastically rigid object) can pose challenges to such approaches. Additionally, these approaches increase in algorithmic complexity as they typically involve two solvers—one for the fluid and one for the solid—whose complexity increases even more so when incorporating viscoelasticity. Additionally, the Lagrangian portion of the numerical approach of the solver is typically limited in its ability to capture high-frequency contents of relevant waves relative to the Eulerian counterpart. Thus, our present focus resides in the latter—a single framework for fluids and solids, which can represent fully coupled fluid–solid mechanics. Given our interest in leveraging the advantages of high-order shock- and interface-capturing approaches, the chief difficulty lies in representing strains (or deformations), naturally described in a Lagrangian fashion, in the Eulerian formulation of predilection for discontinuity capturing. This difficulty has been addressed primarily by following either Godunov-based or "conventional" approaches [25].

In the Godunov-based approach, the deformation tensor is directly evolved, such that the equations of motion form a hyperbolic, conservative, and thermodynamically consistent set of equations [26,80,63,27]. Hyperelastic constitutive models, which depend on the deformation tensor, can thus be represented using this approach. Computational studies of shocks in a single elastic medium were performed with second-order shock-capturing schemes [44,54,52,53,25]. High-order Weighted Essentially Non-Oscillatory (WENO) [33], Arbitrary DERivative in space and time (ADER) [75] and Discontinuous Galerkin approaches have been implemented for single-phase problems involving fluids and solids [19]. These methods can represent interfaces via interface tracking and capturing, as well as immersed boundary methods [10,12,9,71,49,50,28]. However, these interface-tracking techniques may suffer conservation losses. Although interface capturing, e.g., using the seven- or five-equations multiphase models [7,41,67,69], has been used for ballistic and detonation problems [22,21,57,58] with second-order accurate schemes, the implementation of Riemann solvers appropriately capturing all the waves of the nonlinear hyperbolic systems for arbitrary constitutive models is challenging. Moreover, it is not clear how to incorporate stress relaxation in such a formulation.

For these reasons, we consider conventional approaches, in which an objective temporal derivative of the constitutive relation is performed to obtain an evolution equation for the stress tensor. This process effectively transforms strains into strain rates, which can naturally be represented in an Eulerian formulation in terms of the velocity gradient [43,18]. Moreover, this process is suited to hypoelastic constitutive models for small strains [20] in which the elastic components of the stress tensor obey evolution equations. Appropriate objective derivatives must be used, e.g., Lie derivative [5]; if not, thermodynamically inconsistent equations and results may be obtained [80,55]. The resulting system of equations is attractive given the relatively straightforward numerical implementation of viscoelasticity, including generalized Zener models [65]. This conventional approach has been used in the geophysical community to simulate nonlinear wave propagation in viscoelastic media [14]. For multi-material problems, the ADER scheme was implemented to investigate wave propagation in incompressible viscoelastic media using an immersed interface method, with a specific focus on stress relaxation [48]. The Sharp-Interface approach, a mixed Eulerian–Lagrangian method [81], and the particle level-set method [77] have been used to study high-speed solid impact, penetration and void collapse problems [78,79]. The Ghost Fluid method has also been employed to simulate elastic–plastic deformations [38,37,40,39]. However, interface capturing (e.g., five-equations model) has yet to be used in conjunction with this conventional approach. Interface capturing can be designed to be fully conservative, by contrast to the tracking methods described above. However, one of the expected challenges when using interface capturing in conjunction with this conventional approach, which we address, lies in maintaining the appropriate interfacial conditions and preventing spurious pressure and temperature errors [1,68,34,2].

Our goal is to develop a numerical method capable of accurately representing wave propagation (including shocks and other high-frequency-content waves) in heterogeneous and compressible viscoelastic media with interfaces and heat diffusion processes. Given our interest in problems in which solid deformations are sufficiently small and exhibit elastic, viscous and memory effects (stress relaxation), the key contribution in this article is to extend the five-equations interface-capturing method for compressible multiphase flows to the generalized Zener linear viscoelastic model (i.e., with elasticity and relaxation) based on the Lie derivative. In this fully coupled fluid–solid approach, all materials (gases, liquids, solids) obey the same equation of state and constitutive model with spatially varying properties. Such an approach is attractive since the same numerical scheme can be applied throughout the computational domain; furthermore, we can leverage high-order accurate discontinuity-capturing schemes commonly used in Eulerian calculations. The article is organized as follows. We first present our physical model, with an emphasis on the constitutive relations. We then describe our numerical model and analyze the properties of the system of equations. Next, the numerical method is discussed. A stringent suite of one- and two-dimensional, single- and multi-phase test problems with various viscoelastic models, shocks and interfaces, is presented for verification purposes.

2. Physical model

2.1. Equations of motion

The equations governing the phenomena of interest are the mass conservation, momentum balance and energy balance equations:

$$\frac{\partial \rho}{\partial t} + \frac{\partial}{\partial x_j}(\rho u_j) = 0, \tag{1a}$$

$$\frac{\partial}{\partial t}(\rho u_i) + \frac{\partial}{\partial x_j}(\rho u_i u_j - \sigma_{ij}) = 0, \tag{1b}$$

$$\frac{\partial E}{\partial t} + \frac{\partial}{\partial x_j}(E u_j - \sigma_{ij} u_i) = -\frac{\partial Q_k}{\partial x_k}, \tag{1c}$$

$$\frac{\partial}{\partial t}(\rho^{(k)}\alpha^{(k)}) + \frac{\partial}{\partial x_j}(\rho^{(k)}\alpha^{(k)} u_j) = 0, \qquad k = 1, ..., K-1, \tag{1d}$$

where ρ is the total density, u_i the velocity vector, σ_{ij} the Cauchy stress tensor, Q_k the heat flux, $\alpha^{(k)}$ the volume fraction of material k, K the total number of materials, and indices $i, j = 1, 2$, and 3. Repeated indices imply summation. Eqs. (1d) are mass conservation equations for $K-1$ materials. The total energy (per unit volume) E comprises internal, kinetic and elastic contributions:

$$E = \rho e + \frac{1}{2}\rho u_i^2 + \rho e^{(e)}. \tag{2}$$

The internal energy (per unit volume) ρe is related to the relevant thermodynamic quantities through the equation of state described in the next section, and the elastic energy $\rho e^{(e)}$ is described in more detail in §2.3. Material k has volume fraction $\alpha^{(k)}$ and density $\rho^{(k)}$, with

$$\sum_k \rho^{(k)}\alpha^{(k)} = \rho, \qquad \sum_k \alpha^{(k)} = 1. \tag{3}$$

As described in §3.2, $K-1$ mass balance equations, corresponding to the K materials, must be evolved.

2.2. Equation of state

The Noble–Abel Stiffened-Gas equation of state [46] is used to relate the internal energy to pressure and temperature in all materials:

$$\rho e = \frac{p(1 - \rho b)}{n - 1} + \frac{nB(1 - \rho b)}{n - 1} + \rho q \tag{4a}$$

$$= \rho cT + B(1 - \rho b) + \rho q, \tag{4b}$$

where T is the temperature and q, n, B, b and c are material properties prescribed to produce the correct propagation speeds in liquids and solids [30,45,46]. This equation reduces to the stiffened gas equation of state [45] with $b = 0$ and by setting the other properties to appropriate values. In the limit of ideal gases, $B = 0$, $b = 0$, $q = 0$, c is the specific heat at constant volume and $n = \gamma$ is the ratio of specific heats. Table 1 lists the values of the material properties corresponding to materials of interest. The model viscoelastic medium has properties very similar to those of water, with a slightly greater acoustic impedance. The calculation of ρe when multiple materials are present is discussed in §3.2.

2.3. Constitutive relations

Closure relationships for the heat flux and Cauchy stress tensor are required to close the system of equations. Fourier conduction describes the heat diffusion process:

Table 1
Material properties corresponding to different media described by the Noble–Abel Stiffened-Gas equation of state.

Material	n	b [m³/kg × 10⁻⁴]	B [Pa × 10⁶]	q [kJ/kg]	c [kJ/kg · K]
Air	1.40	0	0	0	0.718
Water & viscoelastic medium	1.19	6.61	702.8	−1.167	4.167

$$Q_k = -\kappa \frac{\partial T}{\partial x_k}, \tag{5}$$

where κ is the thermal conductivity.

Before discussing the stresses, we define the strain-rate tensor and its deviatoric part,

$$\dot{\epsilon}_{ij} = \frac{1}{2}\left(\frac{\partial u_i}{\partial x_j} + \frac{\partial u_j}{\partial x_i}\right), \qquad \dot{\epsilon}_{ij}^{(d)} = \dot{\epsilon}_{ij} - \frac{1}{3}\dot{\epsilon}_{kk}\delta_{ij}, \tag{6}$$

where the dot denotes an objective temporal derivative, here the Lie derivative. The Cauchy stress tensor can be written in terms of isotropic and deviatoric contributions,

$$\sigma_{ij} = \sigma_{ij}^{(i)} + \tau_{ij}^{(d)}. \tag{7}$$

The isotropic term consists of mechanical pressure and bulk (dilatational) viscous contributions:

$$\sigma_{ij}^{(i)} = -p\delta_{ij} + \mu_b \dot{\epsilon}_{kk}\delta_{ij}, \tag{8}$$

where μ_b is the bulk viscosity. The isotropic elastic contributions to the Cauchy stress tensor, which are associated with density changes in the material, are captured via the mechanical pressure, which itself is determined through the equation of state.

The deviatoric stress can further be written in terms of viscous, $\tau_{ij}^{(v)}$, and elastic, $\tau_{ij}^{(e)}$, contributions,

$$\tau_{ij}^{(d)} = \tau_{ij}^{(v)} + \tau_{ij}^{(e)}, \tag{9}$$

where $\tau_{ij}^{(v)} = 2\mu_s \dot{\epsilon}_{ij}^{(d)}$. The elastic stress is modeled as a hypoelastic material where the stress tensor rate linearly depends on the spatial velocity gradient [20],

$$\dot{\tau}_{ij}^{(e)} = \mathcal{D}_{ijkl}\frac{\partial u_k}{\partial x_l}, \tag{10}$$

where $\mathcal{D}_{ijkl}$ is a rank-4 tensor with the objective stress tensor rate terms. Since we consider isotropic media, $\tau_{ij}^{(e)} = 2G\epsilon_{ij}^{(d)}$. Our focus lies in materials that may exhibit stress relaxation, elasticity and viscosity, and undergo infinitesimally small deformations (i.e., linear viscoelasticity in which the stress and its rate depend linearly on the strain and its rate). The simplest constitutive model accounting for these effects is the Zener model [86], used to represent, among other things, biomaterials [24]:

$$\lambda_r \dot{\tau}_{ij}^{(d)} + \tau_{ij}^{(d)} = 2\mu_s \dot{\epsilon}_{ij}^{(d)} + 2G\epsilon_{ij}^{(d)}, \tag{11}$$

where λ_r is the relaxation time, μ_s the shear viscosity, G the shear modulus. The elastic energy is then defined as

$$\rho e^{(e)} = \frac{\tau_{ij}^{(e)}\tau_{ij}^{(e)}}{4G}. \tag{12}$$

The Zener model has the advantage of reducing to other simple linear constitutive relations [15,24,84]. For $\lambda_r = 0$, the model reduces to that representing a Kelvin–Voigt solid,

$$\tau_{ij}^{(d)} = 2\mu_s \dot{\epsilon}_{ij}^{(d)} + 2G\epsilon_{ij}^{(d)}. \tag{13}$$

If $\mu_s = 0$ and $\lambda_r = 0$, the model further reduces to that representing a linear Hookean solid,

$$\tau_{ij}^{(d)} = 2G\epsilon_{ij}^{(d)}. \tag{14}$$

In Eq. (11), the model represents a Maxwell fluid if $G = 0$,

$$\lambda_r \dot{\tau}_{ij}^{(d)} + \tau_{ij}^{(d)} = 2\mu_s \dot{\epsilon}_{ij}^{(d)}. \tag{15}$$

Additionally, if $\lambda_r = 0$, the model further reduces to that representing a viscous, Newtonian fluid,

$$\tau_{ij}^{(d)} = 2\mu_s \dot{\epsilon}_{ij}^{(d)}. \tag{16}$$

The Zener model can further be generalized to account for materials exhibiting frequency-dependent viscoelastic properties, e.g., soft tissue [42,60]. The shear relaxation function is defined as [15],

$$\psi = G_r \left(1 + \sum_{l=1}^{N_r} \varsigma^{(l)} \exp(-\theta^{(l)}t)\right) H(t), \tag{17}$$

where G_r is the relaxed shear modulus, $\varsigma^{(l)}$ the strictly positive relaxation shear coefficient corresponding to relaxation frequency $\theta^{(l)}$, N_r the total number of frequencies and $H(t)$ the Heaviside function. The elastic stress can be written as a time convolution of the shear relaxation function and (deviatoric) strain rate,

$$\tau_{ij}^{(d)} = 2\psi(t) * \epsilon_{ij}^{(d)}. \tag{18}$$

3. Numerical model

3.1. Numerical implementation of viscoelastic models

3.1.1. Kelvin–Voigt

We first consider the Kelvin–Voigt model, perhaps the simplest viscoelastic model in which an elastic contribution is simply added to the viscous stress to form the total deviatoric stress. Drawing from [43,5,4], the Lie objective temporal derivative of the elastic stress is taken to transform strains into strain rates,

$$\dot{\tau}_{ij}^{(e)} = \frac{\partial \tau_{ij}^{(e)}}{\partial t} + u_k \frac{\partial \tau_{ij}^{(e)}}{\partial x_k} - \tau_{kj}^{(e)} \frac{\partial u_i}{\partial x_k} - \tau_{ik}^{(e)} \frac{\partial u_j}{\partial x_k} + \tau_{ij}^{(e)} \frac{\partial u_k}{\partial x_k}, \tag{19}$$

where the first two terms are the material derivative of the stress tensor and the rest of the terms contribute to preserving objectivity. The material derivative is incorporated in the Lie derivative to transport elastic stress tensor discontinuities. We note that the Lie derivative is equivalent to the Truesdell derivative [5] in a rectangular Cartesian coordinate system. We follow the restrictions for the thermodynamic consistency of the Truesdell derivative [55]. The Oldroyd derivative is obtained if the last term in Eq. (19) is set to zero. These stress rates, among others, and their behavior under small and finite deformations have been characterized in the literature [74].

Another useful property of the Lie derivative is that its acoustic tensor is symmetric. The acoustic tensor is defined as

$$\mathcal{A}_{jk} = \frac{1}{\rho} n_i \left(\mathcal{B}_{ijkl} + \mathcal{C}_{ijkl} \right) n_l, \tag{20}$$

where n_i is an arbitrary unit vector, $\mathcal{B}_{ijkl}$ the tensor of objective stress rates, and $\mathcal{C}_{ijkl}$ the stiffness tensor,

$$\dot{\tau}_{ij}^{(e)} = \mathcal{C}_{ijkl} \frac{\partial u_k}{\partial x_l} = 2G \left(\mathcal{I}_{ijkl} - \frac{1}{3}\delta_{ij}\delta_{kl} \right) \frac{\partial u_k}{\partial x_l} = 2G\dot{\epsilon}_{ij}^{(d)}, \tag{21}$$

where $\mathcal{I}_{ijkl}$ is the rank-4 identity tensor and the final equality holds for an isotropic medium. The acoustic tensor for the Lie derivative can thus be written,

$$\mathcal{A}_{jk} = \frac{1}{\rho} n_i \left(\mathcal{B}_{ijkl} + \mathcal{C}_{ijkl} \right) n_l = \frac{1}{\rho} \left[n_i \tau_{il}^{(e)} n_l \delta_{jk} + G \left(\delta_{jk} + \frac{n_j n_k}{3} \right) \right], \tag{22}$$

which is symmetric, by contrast to the Jaumann derivative [80].

Combining mass conservation and Eqs. (19) and (21), the evolution equation using the Lie derivative for the elastic stress tensor becomes

$$\frac{\partial}{\partial t}(\rho \tau_{ij}^{(e)}) + \frac{\partial}{\partial x_k}(\rho \tau_{ij}^{(e)} u_k) = \rho \left(\tau_{kj}^{(e)} \frac{\partial u_i}{\partial x_k} + \tau_{ik}^{(e)} \frac{\partial u_j}{\partial x_k} - \tau_{ij}^{(e)} \frac{\partial u_k}{\partial x_k} + 2G\dot{\epsilon}_{ij}^{(d)} \right). \tag{23}$$

In two dimensions, three equations must be solved for the elastic contribution of the stress, namely for $\tau_{11}^{(e)}$, $\tau_{22}^{(e)}$ and $\tau_{12}^{(e)}$ (or $\tau_{21}^{(e)}$, since the Cauchy stress tensor is symmetric). In the absence of elastic effects (i.e., $G = 0$), the compressible Navier–Stokes equations are recovered. In the absence of viscous effects (i.e., $\mu_s = \mu_b = 0$), the Euler equations with elastic stresses are recovered [43,25,37,40]. Eq. (23) complements the mass, momentum and energy Eqs. (1). The momentum and energy equations are solved as follows:

$$\frac{\partial}{\partial t}(\rho u_i) + \frac{\partial}{\partial x_j}(\rho u_i u_j + p\delta_{ij} - \tau_{ij}^{(e)}) = \frac{\partial}{\partial x_j} \left(\tau_{ij}^{(v)} + \mu_b \dot{\epsilon}_{kk}\delta_{ij} \right), \tag{24a}$$

$$\frac{\partial E}{\partial t} + \frac{\partial}{\partial x_j}[(E+p)u_j - \tau_{ij}^{(e)} u_i] = \frac{\partial}{\partial x_j} \left[u_i \left(\tau_{ij}^{(v)} + \mu_b \dot{\epsilon}_{kk}\delta_{ij} \right) \right] + \frac{\partial}{\partial x_j} \left(\kappa \frac{\partial T}{\partial x_j} \right). \tag{24b}$$

The model equations for Kelvin–Voigt using the Lie derivative implementation for stress evolution are Eqs. (1a), (1d), (23) and (24).

3.1.2. Zener and generalized Zener model

For the Zener and generalized Zener models, we extend the differential viscoelastic model in [65,13,48] to incorporate the constitutive model, Eq. (18). We follow the thermodynamic restrictions for the Zener model [82]. Following the same procedure as that described in the previous section, a Lie derivative of the constitutive relation is taken to transform the strains into strain rates, thus yielding the following equations for the stress and memory variables:

$$\frac{\partial}{\partial t}\left(\rho \tau_{ij}^{(e)}\right) + \frac{\partial}{\partial x_j}(\rho \tau_{ij}^{(e)} u_j) = \rho \left[\tau_{kj}^{(e)} \frac{\partial u_i}{\partial x_k} + \tau_{ik}^{(e)} \frac{\partial u_j}{\partial x_k} - \tau_{ij}^{(e)} \frac{\partial u_k}{\partial x_k} + 2G\dot{\epsilon}_{ij}^{(d)} + \sum_{l}^{N_r} \xi_{ij}^{(l)} \right], \tag{25a}$$

$$\frac{\partial}{\partial t}(\rho \xi_{ij}^{(l)}) + \frac{\partial}{\partial x_j}(\rho \xi_{ij}^{(l)} u_j) = \rho \left[\xi_{kj}^{(l)} \frac{\partial u_i}{\partial x_k} + \xi_{ik}^{(l)} \frac{\partial u_j}{\partial x_k} - \xi_{ij}^{(l)} \frac{\partial u_k}{\partial x_k} - \theta^{(l)}\left(2\varsigma^{(l)} G_r \dot{\epsilon}_{ij}^{(d)} + \xi_{ij}^{(l)} \right) \right], \quad l = 1, ..., N_r, \tag{25b}$$

where $\xi_{ij}^{(l)}$ is the lth memory variable,

$$\xi_{ij}^{(l)} = -\theta^{(l)} G_r \varsigma^{(l)} \exp(-\theta^{(l)} t) H(t) \star \dot{\epsilon}_{ij}^{(d)}, \tag{26}$$

G_r is the relaxed shear modulus,

$$G = G_r \left(1 + \sum_{l=1}^{N_r} \varsigma^{(l)} \right), \tag{27}$$

and $\varsigma^{(l)}$ are the strictly positive relaxation coefficients for the given material which can be obtained by material characterization [48]. Using the mechanical analog of the generalized Zener model [15], the relaxation coefficients can be evaluated using material properties,

$$\varsigma^{(l)} = \lambda_\epsilon^{(l)} \theta^{(l)} - 1, \tag{28}$$

where $\lambda_\epsilon^{(l)}$ are the retardation times, or creep times. There are N_r relaxation frequencies corresponding to N_r memory variables and evolution equations. The additional evolution equations close the system without having to perform a convolution in time, i.e., Eq. (26) need not be solved. The model equations for the generalized Zener model using the Lie derivative implementation for stress transport are Eqs. (1a), (1d), (24), and (25). These equations close the momentum and energy balance equations, Eqs. (24). We note that Eq. (25) incorporates the shear viscous contributions and that both the retardation and relaxation times are functions of the shear viscosity. Thus, the $\tau_{ij}^{(v)}$ term solved in the conservation of linear momentum and energy equations, i.e., Eqs. (24), should not be included when solving for the Zener, generalized Zener, and Maxwell models. However, the bulk viscosity contributions in Eq. (8) must be retained in this formulation. If there is only one relaxation time (i.e., $N_r = 1$), we recover the Zener model. For a single relaxation frequency, the Maxwell model is recovered by setting $G = G_r = \mu_s \theta^{(1)}$. In the absence of elasticity and relaxation, the model reverts to the Newtonian model in Eqs. (24), in which case Eqs. (25) need not be solved, $\tau_{ij}^{(e)}$ terms are neglected, and $\tau_{ij}^{(v)}$ must be included in Eqs. (24).

3.1.3. Eigensystem of the Euler equations with hypoelastic stresses using the Lie derivative

The eigensystem of the Euler equations are well known. For a hypoelastic medium with a Lie derivative implementation, additional terms are present. Here, we determine how elasticity and the additional terms introduced by the Lie derivative affect the eigensystem. We neglect viscous and thermal effects, and consider the one-dimensional equations for a single material,

$$\frac{\partial \rho}{\partial t} + \frac{\partial}{\partial x}(\rho u) = 0,$$

$$\frac{\partial}{\partial t}(\rho u) + \frac{\partial}{\partial x}(\rho u^2 + p - \tau_{11}^{(e)}) = 0,$$

$$\frac{\partial}{\partial t}(\rho v) + \frac{\partial}{\partial x}(\rho v u - \tau_{12}^{(e)}) = 0,$$

$$\frac{\partial E}{\partial t} + \frac{\partial}{\partial x}\left[u(E + p - \tau_{11}^{(e)}) - v\tau_{12}^{(e)} \right] = 0,$$

$$\frac{\partial}{\partial t}(\rho \tau_{11}^{(e)}) + \frac{\partial}{\partial x}(\rho u \tau_{11}^{(e)}) = \rho \left(\frac{4G}{3} + \tau_{11}^{(e)} \right) \frac{\partial u}{\partial x}, \tag{29}$$

$$\frac{\partial}{\partial t}(\rho \tau_{22}^{(e)}) + \frac{\partial}{\partial x}(\rho u \tau_{22}^{(e)}) = \rho \left(-\frac{2G}{3} - \tau_{22}^{(e)} \right) \frac{\partial u}{\partial x} + 2\rho \tau_{12}^{(e)} \frac{\partial v}{\partial x},$$

$$\frac{\partial}{\partial t}(\rho \tau_{12}^{(e)}) + \frac{\partial}{\partial x}(\rho u \tau_{12}^{(e)}) = \rho \left(G + \tau_{11}^{(e)} \right) \frac{\partial v}{\partial x},$$

which can be written in quasi-linear form,

$$\frac{\partial W}{\partial t} + A(W)\frac{\partial W}{\partial x} = 0, \tag{30}$$

where W is the vector of primitive variables and A is the Jacobian matrix,

$$W = \begin{bmatrix} \rho \\ u \\ v \\ p \\ \tau_{11}^{(e)} \\ \tau_{22}^{(e)} \\ \tau_{12}^{(e)} \end{bmatrix}, \qquad A(W) = \begin{bmatrix} u & \rho & 0 & 0 & 0 & 0 & 0 \\ 0 & u & 0 & \frac{1}{\rho} & -\frac{1}{\rho} & 0 & 0 \\ 0 & 0 & u & 0 & 0 & 0 & -\frac{1}{\rho} \\ 0 & \rho a^2 & 0 & u & 0 & 0 & 0 \\ 0 & -\frac{4G}{3} - \tau_{11}^{(e)} & 0 & 0 & u & 0 & 0 \\ 0 & \frac{2G}{3} + \tau_{22}^{(e)} & -2\tau_{12}^{(e)} & 0 & 0 & u & 0 \\ 0 & 0 & -G - \tau_{11}^{(e)} & 0 & 0 & 0 & u \end{bmatrix}, \tag{31}$$

where $a = \sqrt{\frac{n(p+B)}{\rho(1-\rho b)}}$ is the speed of sound corresponding to the Noble–Abel Stiffened-Gas equation of state. The eigenvalues (i.e., wave speeds) of the Jacobian matrix are:

$$\zeta_{1,2,3} = u, \quad \zeta_{4,5} = u \pm \sqrt{\frac{G + \tau_{11}^{(e)}}{\rho}}, \quad \zeta_{6,7} = u \pm \sqrt{a^2 + \frac{4G/3 + \tau_{11}^{(e)}}{\rho}}. \tag{32}$$

For the analysis in the y-direction, u and $\tau_{11}^{(e)}$ in the eigenvalues in Eq. (32) are replaced with v and $\tau_{22}^{(e)}$, respectively. As expected, the presence of elasticity manifests in the characteristic wave speeds by two important modifications: it introduces three additional waves (a linearly degenerate wave ζ_5 and two shear waves $\zeta_{4,5}$) and it increases the propagation speed of the (longitudinal) pressure waves. If the analysis is extended to the Zener model, there are three additional linearly degenerate waves; for the generalized Zener model, each additional relaxation frequency introduces three additional such waves. When considering multi-material problems, each additional material introduces a linearly degenerate wave. In the absence of elasticity, the speed of sound reduces to that expected for a fluid obeying the Noble–Abel Stiffened-Gas equation of state.

The corresponding right eigenvector matrix of the Jacobian matrix,

$$R = \begin{bmatrix} 0 & 0 & 1 & 0 & 0 & \rho & \rho \\ 0 & 0 & 0 & 0 & 0 & \sqrt{a^2 + \frac{4G/3 + \tau_{11}^{(e)}}{\rho}} & -\sqrt{a^2 + \frac{4G/3 + \tau_{11}^{(e)}}{\rho}} \\ 0 & 0 & 0 & -\sqrt{\frac{G + \tau_{11}^{(e)}}{\rho}} & \sqrt{\frac{G + \tau_{11}^{(e)}}{\rho}} & 0 & 0 \\ 0 & 1 & 0 & 0 & 0 & \rho a^2 & \rho a^2 \\ 0 & 1 & 0 & 0 & 0 & -(4G/3 + \tau_{11}^{(e)}) & -(4G/3 + \tau_{11}^{(e)}) \\ 1 & 0 & 0 & 2\tau_{12}^{(e)} & 2\tau_{12}^{(e)} & 2G/3 + \tau_{22}^{(e)} & 2G/3 + \tau_{22}^{(e)} \\ 0 & 0 & 0 & G + \tau_{11}^{(e)} & G + \tau_{11}^{(e)} & 0 & 0 \end{bmatrix}, \tag{33}$$

where the j-th column corresponds to the j-th wave speed ζ_j. We recognize the three linearly degenerate waves in the first three columns, with the first and third corresponding to the $\tau_{22}^{(e)}$ and density jump across the contact, respectively, and the second to $\sigma_{11} = (-p + \tau_{11}^{(e)})$, which is continuous across the contact. Then come the s-waves (shear) in the fourth and fifth columns, followed by the p-waves (pressure) in the sixth and seventh columns. We further note that the i-th primitive variable is discontinuous across the j-th wave if the entry in the i-th row and j-th column is non-zero. This observation is particularly important for the shear waves, where this analysis indicates that v, $\tau_{22}^{(e)}$ and $\tau_{12}^{(e)}$ are discontinuous when using the Lie derivative.

3.2. Multi-material framework

We extend the five-equations compressible multiphase model [3,56,2] used to capture gas/liquid material interfaces to solids. In this framework, all the materials (gases, liquids, solids) obey the same equation of state and constitutive relations, with spatially varying material properties; numerical dissipation at interfaces gives rise to a (numerical) mixture region in which appropriate rules must be specified to prevent spurious errors at interfaces. In addition to the total mass conservation equation (1a), $K - 1$ species conservation equations are solved in both conservative form as in Eq. (1d) and in non-conservative form to maintain interfacial equilibrium conditions for velocity, pressure and temperature [2],

$$\frac{\partial \alpha^{(k)}}{\partial t} + u_j \frac{\partial \alpha^{(k)}}{\partial x_j} = \Gamma^{(k)} \frac{\partial u_j}{\partial x_j}, \tag{34}$$

where $k = 1, ..., K - 1$ and

$$\Gamma^{(k)} = \frac{\alpha^{(k)}}{K_s^{(k)}} \left(\frac{1}{\sum_l \frac{\alpha^{(l)}}{K_s^{(l)}}} - K_s^{(k)} \right), \qquad K_s^{(k)} = \rho^{(k)} (a^{(k)})^2 = \frac{n^{(k)}(p + B^{(k)})}{(1 - \rho^{(k)} b^{(k)})}. \tag{35}$$

The right-hand-side of this equation is sometimes set to zero [3,51,56,62,72]; however, this term is necessary to accurately represent compressible multiphase problems.

The pressure and temperature are computed based on the internal energy as follows:

$$p = \frac{E - \rho \frac{u_i^2}{2} - \rho e^{(e)} - \sum_k \rho^{(k)} \alpha^{(k)} q^{(k)} - \sum_k \alpha^{(k)} \frac{n^{(k)} B^{(k)} (1 - \rho^{(k)} b^{(k)})}{n^{(k)} - 1}}{\sum_k \alpha^{(k)} \frac{1}{n^{(k)} - 1}}, \tag{36a}$$

$$T = \frac{E - \rho \frac{u_i^2}{2} - \rho e^{(e)} - \sum_k \rho^{(k)} \alpha^{(k)} q^{(k)} - \sum_k \alpha^{(k)} (1 - \rho^{(k)} b^{(k)}) B^{(k)}}{\sum_k \rho^{(k)} \alpha^{(k)} c^{(k)}}, \tag{36b}$$

where terms with $\rho^{(k)} \alpha^{(k)}$ are calculated using Eq. (1d), terms with $\alpha^{(k)}$ only are calculated using Eq. (34), as described in [2]. Thus, the internal energy equation is calculated as follows,

$$\rho e = p \sum_k \alpha^{(k)} \frac{(1 - \rho^{(k)} b^{(k)})}{n^{(k)} - 1} + \sum_k \alpha^{(k)} \frac{n^{(k)} B^{(k)} (1 - \rho^{(k)} b^{(k)})}{n^{(k)} - 1} + \sum_k \rho^{(k)} \alpha^{(k)} q^{(k)}, \quad \text{(pressure} - \text{wise)}, \tag{37}$$

$$= T \sum_k \rho^{(k)} \alpha^{(k)} c^{(k)} + \sum_k \alpha^{(k)} B^{(k)} (1 - \rho^{(k)} b^{(k)}) + \sum_k \rho^{(k)} \alpha^{(k)} q^{(k)}, \qquad \text{(temperature} - \text{wise)}. \tag{38}$$

For simplicity and without loss of generality, mixture material properties ϕ (e.g., moduli, viscosities, thermal conductivity, etc.) are weighted by the volume fraction:

$$\phi = \sum_k \alpha^{(k)} \phi^{(k)}. \tag{39}$$

4. Numerical method

Without loss of generality, we consider the one-dimensional form of the equations,

$$\left. \frac{dU}{dt} \right|_i = -\frac{F_{i+1/2} - F_{i-1/2}}{\Delta x} + D_i(U) + S_i(U), \tag{40}$$

where U denotes the conservative variables, F the convective flux, the D diffusion operator and S source terms. Our overall approach is based on explicit finite differences in space and explicit time-marching.

4.1. Temporal discretization

For time marching, we use the standard explicit fourth-order Runge–Kutta scheme. The time-step constraint is calculated by accounting for advection and diffusion,

$$\Delta t = \min \left(\nu \frac{\Delta x}{\zeta_{max}}, \nu_\mu \frac{\Delta x^2}{(\mu_s / \rho)}, \nu_\kappa \frac{\Delta x^2}{(\kappa / \rho c)} \right), \tag{41}$$

where Δx is the mesh size, ζ_{max} the maximum wave speed in the system (and computational domain), ν is the Courant number, ν_μ and ν_r are the von Neumann numbers for viscous and thermal diffusion. We set $\nu = 0.85$, $\nu_\mu = \nu_\kappa = 0.125$.

Since $G \geq 0$, the maximum wave speed is calculated, as shown from the analysis in §3.1.3, as follows:

$$\zeta_{max} = \max_j \left(|u| \pm \sqrt{\frac{n(p + B)}{\rho(1 - \rho b)} + \frac{4G/3 + \tau_{jj}^{(e)}}{\rho}} \right)_j. \tag{42}$$

4.2. Spatial discretization

The spatial discretization is based on a solution-adaptive approach that introduces numerical dissipation only where necessary. The discontinuity sensor of [32,2] detects shocks, contact discontinuities and material interfaces, such that the convective fluxes are computed as follows:

$$F_{i\pm 1/2} = bF_{i\pm 1/2}|_{central} + (1-b)F_{i\pm 1/2}|_{HLL}, \tag{43}$$

where the subscripts "central" and "HLL" are explained below, $b = 1$ is smooth regions and $b = 0$ at discontinuities. The function

$$\Phi_A = \frac{4\phi_A}{(1+\phi_A)^2}, \qquad \phi_A = \frac{|A_R - A_L|}{A_R + A_L}, \tag{44}$$

where A is p, ρ or n, and L and R denote the left and right edge of a computational cell, is evaluated. If $\Phi_A > 0.0001 \ \forall A$ in a given cell, the solution therein is considered discontinuous and the WENO approach of [36] is used for all the primitive variables along with the HLL Riemann solver [31] with appropriate correction for equations in non-conservative form [68]; in a finite-difference framework, this scheme is formally second-order accurate, but since it is applied at discontinuities only it does not affect the overall convergence rate. Otherwise, standard fourth-order explicit central differences are applied. In the diffusion and source terms, the derivatives are computed using explicit fourth-order central differences; if material properties are variable, their derivatives are calculated in non-conservative form. When solving Eq. (34) with the source term, the numerical method's stiffness is significantly increased and, thus, the criterion $\Phi_A > 0.0001$ was set to solve the problems of interest. In the absence of the source term, the criterion is less restrictive [2]. In summary, the overall approach is globally fourth-order accurate in time and space in smooth problems. For problems with discontinuities, the convergence rate reduces to first-order accuracy, as expected. We note however that the fifth-order shock-capturing scheme significantly reduces the amount of dissipation in discontinuous regions.

5. Results

5.1. Wave propagation problem

Without loss of generality, we consider the Kelvin–Voigt model for a single material, i.e., the model viscoelastic medium with properties in Table 1. We non-dimensionalize the problem using a length scale of $L = 1$ mm and the relevant material properties. The thermal conductivity is $\kappa = 0.615$ W/(K m).

Convergence and wave speeds. We use a one-dimensional p-wave (acoustic) problem to verify the convergence rate of the overall scheme and that correct wave speeds are obtained. The initial conditions are

$$(\rho, u, v, p) = (1 + \Delta, 0, \Delta, (1 + nB)/n + \Delta),$$

with $\tau_{11}^{(e)} = \tau_{22}^{(e)} = \tau_{12}^{(e)} = 0$, and where $\Delta = \epsilon \sin^8(\pi x)$, on the periodic domain $x \in [0, 1]$. Values of $\epsilon = 10^{-4}$ and 10^{-1} are used to discriminate between different convergence behaviors. The initial density, pressure and y-velocity split into left- and right-moving waves propagating at speeds $\pm\sqrt{\frac{n(p+B)}{\rho(1-\rho b)} + \frac{4G/3+\tau_{11}^{(e)}}{\rho}}$. For this amplitude, the solution remains smooth throughout such that central differences are always used. The number of grid points is $N = 10, 20, 40, 80$, and 160. The L_2 error, evaluated after one period using the solution on $N = 1024$ as the reference for both Δs, is shown in Fig. 1 in gas ($\mu_b = \mu_s = 0$ and $G = 0$), Newtonian liquid ($\mu_b = \mu_s = 1$ Pa s and $G = 0$), elastic solid ($\mu_b = \mu_s = 0$ and $G = 1$ GPa), and viscoelastic solid ($\mu_b = \mu_s = 1$ Pa s and $G = 1$ GPa). The viscosity and shear modulus are set to these values to demonstrate their effect, if any, on the order of accuracy. For this problem, the Reynolds number is $Re = \rho a L/\mu_s = 1.57 \times 10^3$ and Cauchy number is $Ca = \rho a^2/G = 2.47$. For $\epsilon = 10^{-4}$, the problem remains sufficiently smooth that the sensor never gets activated, such that a fourth-order convergence rate is achieved. For $\epsilon = 10^{-1}$, the amplitude of the perturbation is sufficiently large that the wave steepens such that capturing is activated. As a result, the convergence rate reduces to first-order accuracy. Although not included here, similar results are obtained in a Zener medium (i.e., with relaxation) for both cases.

To verify that the correct wave speeds are obtained as shear modulus is varied, the same problem is considered with $N = 400$, $x \in [0, 2]$, $G = 10^{-6}$, 10^{-3}, 1, 10, 35 and 100 GPa. The viscosities are set to zero. Fig. 2 compares the numerically measured sounds speeds and their theoretical values, $\zeta_{1,2}$. The wave speeds, constant for a given modulus, are obtained by tracking the x-location and time of the peak density, and are scaled by the reference sound speed in the viscoelastic medium with $G = 0$, a_0. As the shear modulus is increased, the wave speed increases accordingly. The agreement is excellent for all values of G under consideration.
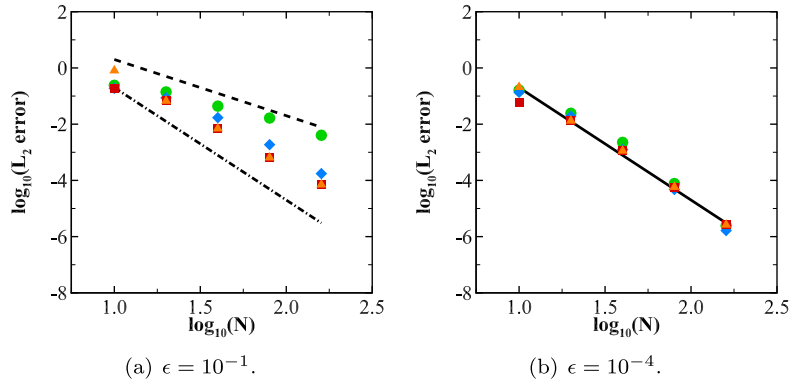
Fig. 1. L_2 error in pressure for the 1D wave-propagation problem. Green circles: gas ($\mu_b = \mu_s = 0$, $G = 0$); blue diamonds: Newtonian liquid ($\mu_b = \mu_s = 1$ Pa s, $G = 0$); red squares: elastic solid ($\mu_b = \mu_s = 0$, $G = 1$ GPa); orange triangles: viscoelastic solid ($\mu_b = \mu_s = 1$ Pa s, $G = 1$ GPa); black dashed line: -1 slope; black dashed-dot line: -2 slope; black solid line: -4. (For interpretation of the colors in the figures, the reader is referred to the web version of this article.)
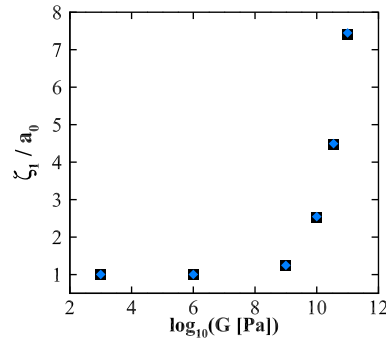
Fig. 2. Comparison of the propagation speed of the p-waves in the 1D wave-propagation problem in a viscoelastic solid between theory (black squares) and simulations (blue diamonds).
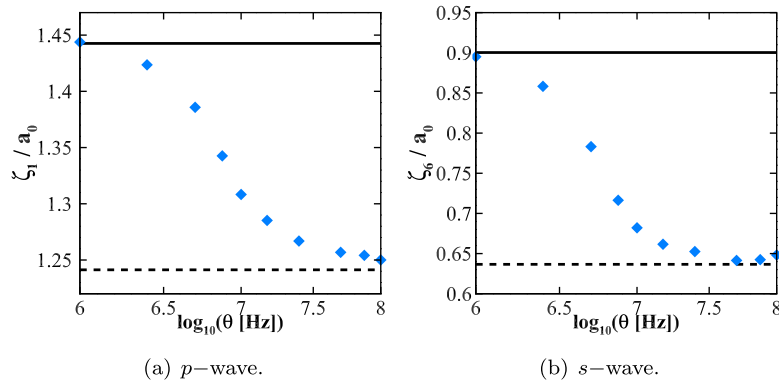
Fig. 3. Dependence of the propagation speed of the p- and s-waves on relaxation frequency for the 1D wave-propagation problem. Black solid line: theoretical wave speed for $G = 2$ GPa; black dotted line: theoretical wave speed for $G_r = 1$ GPa; blue diamonds: Simulation results.

Effects of relaxation on p- and s-wave propagation. We verify the implementation of relaxation effects and frequency dependence using the generalized Zener model. Without loss of generality, we consider a single relaxation time and compute the same problem, with $N = 600$, $x \in [-1.5, 1.5]$ to obtain both the p- and s-waves. The initial single memory variable is set $\xi_{11}^{(1)} = \xi_{22}^{(1)} = \xi_{12}^{(1)} = 0$. The viscosities are also set to zero. The relaxation frequency is varied such that $\theta^{(1)} \in [1, 100]$ MHz, with a relaxation coefficient of $\varsigma^{(1)} = 1$ and $G = 2$ GPa, $G_r = 1$ GPa, all consistent with Eq. (27). The dependence of the p- and s-waves on relaxation is shown in Fig. 3, with the waves calculated as described above using a least-squares fit by tracking the corresponding wave amplitude, and scaled by a_0. The results are as expected. At the lowest relaxation frequen-

cies, the wave speeds agree with those corresponding to an unrelaxed shear modulus of $G = 2$ GPa. As the frequency is increased, the wave speeds decrease to reach the limit of the relaxed shear modulus at infinite frequency.

5.2. Material interface advection problem – interfacial conditions

We demonstrate that an extension of the five-equations multiphase model to viscoelasticity can be performed while preserving the appropriate interfacial conditions [1,73,34,2]. We adapt the 1D gas–liquid interface problem in [2], replacing the liquid by a viscoelastic solid described by a Kelvin–Voigt model with the material properties of the model viscoelastic medium in Table 1. The initial conditions are

$$(\rho, u, v, p) = \begin{cases} (1, 0.5, 0.5, 1/\gamma), & \text{if } x/L \in [0.25, 0.75] \\ (1000, 0.5, 0.5, 1/\gamma), & \text{otherwise,} \end{cases} \tag{45}$$

with $\tau_{11}^{(e)} = \tau_{22}^{(e)} = \tau_{12}^{(e)} = 0$ and γ is the n value for air from Table 1, and $L = 1$ mm. A constant, non-zero normal velocity is introduced to magnify any shear errors. The domain, $x \in [0, 1]$, is periodic with $N = 200$. For the model viscoelastic material, $\mu_b = \mu_s = 5$ mPa s, and $G = 1$ MPa and 1 GPa. For air, $\kappa = 0.026$ W/(K m), and for the model viscoelastic material, $\kappa = 0.615$ W/(K m). The density solution, normalized errors in velocities, pressure, temperature and stresses after the solution has traveled four domain lengths are plotted in Fig. 4, and the time history of the errors are included in Fig. 5. Due to fixed precision arithmetic with quantities that differ by several orders of magnitude, the errors are not exactly at the round-off level, but are nevertheless of the similar order as those observed for water in [2]. The largest relative errors (observed in pressure) are on the order of 10^{-7} and remain bounded over time. Much smaller errors are observed for temperature, velocity and stresses. We conclude that our approach preserves the appropriate interface conditions for interface advection problems.

5.3. Elastic medium Riemann problem

We consider three one-dimensional Riemann problems in elastic media taken from [25] to verify the capability of our approach to represent discontinuities: five-wave shock tube, impact, and expansion problems, all for a single material. We evaluate the solution using the Lie derivative implementation. The domain is $x \in [0, 1]$, $L = 1$ mm, and $N = 200$. For comparison's sake, the stiffened gas equation of state is used with $\rho = 1000$ kg/m³, $n = 4.4$ and $B = 600$ MPa. The elastic medium is modeled using the Kelvin–Voigt approach with $G = 10$ GPa and zero viscosities. We compare our results to the analytical solution to elastic Riemann problems of [25]; it is important to note that this "exact" analytical solution strictly applies to problems in which ρG is a constant. For problems in this section, the initial elastic stresses are $\tau_{11}^{(e)} = \tau_{22}^{(e)} = \tau_{12}^{(e)} = 0$.

Five-wave shock tube problem. An initial discontinuity in the tangential velocity (y-component) is superposed onto a pressure jump (1000 : 1) with initial conditions:

$$(\rho, u, v, p) = \begin{cases} (1000, 0, 100, 10^8) & \text{if } x/L \in [0, 0.5], \\ (1000, 0, -100, 10^5) & \text{otherwise.} \end{cases} \tag{46}$$

The solution at $t = 64$ μs is shown in Fig. 6.

Five waves are observed: a right-moving shock, a stationary contact and a left-moving rarefaction (all visible in the density plot), as well as left- and right-propagating shear waves propagating more slowly than the shock and rarefaction, as expected from Eq. (32). At the contact discontinuity, the appropriate interface condition is that the normal stress, $-p + \tau_{11}^{(e)}$, be constant; pressure itself is discontinuous due to the presence of an elastic stress. Overall, our results with the Lie derivative match the analytical solution owing to the relatively small changes in density, i.e., ρG is approximately constant. Based on the eigenanalysis, the correct waves speeds and states are achieved.

Since capabilities to handle large pressure ratios are of interest, we consider the same problem with a higher pressure ratio of $10^5 : 1$, with initial conditions:

$$(\rho, u, v, p) = \begin{cases} (1000, 0, 100, 10^{10}) & \text{if } x/L \in [0, 0.5], \\ (1000, 0, -100, 10^5) & \text{otherwise.} \end{cases} \tag{47}$$

For this problem, $G = 1$ GPa to represent a less stiff material. The solution is plotted at $t = 64$ μs in Fig. 7. The analytical solution assuming constant ρG [25] and the corresponding numerical solution with the Lie derivative exhibit several small differences: the shear wave speeds are slightly different and the values of y-velocity and $\tau_{12}^{(e)}$ are slightly larger between the shear waves. The small overshoots in the x-velocity and pressure just downstream of the shock are attributed to start-up errors [35] and are magnified for this stronger shock represented by the high-order accuracy.
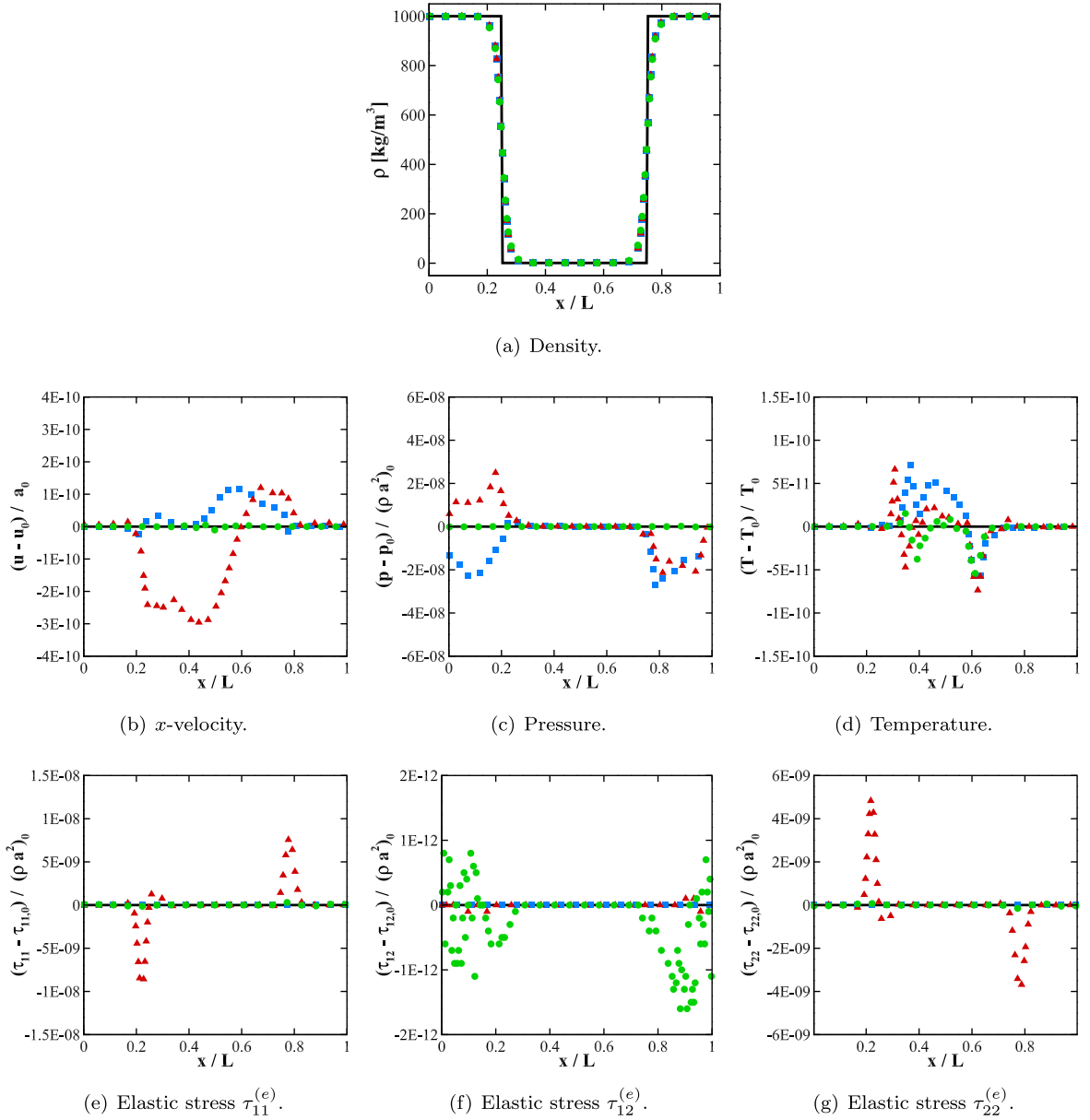
(a) Density.

(b) x-velocity.

(c) Pressure.

(d) Temperature.

(e) Elastic stress $\tau_{11}^{(e)}$.

(f) Elastic stress $\tau_{12}^{(e)}$.

(g) Elastic stress $\tau_{22}^{(e)}$.

Fig. 4. Density solution (a) and relative error (b–g) in the interface advection problem after one period. Blue squares: Newtonian liquid ($G = 0$); red triangles: $G = 1$ MPa; green circles: $G = 1$ GPa; black line: exact solution.

Impact problem. We consider weak ($U = 10$ m/s) and strong ($U = 1000$ m/s) impacts, with initial conditions

$$(\rho, u, v, p) = \begin{cases} (1000, U, 0, 10^5) & \text{if } x/L \in [0, 0.5], \\ (1000, -U, 0, 10^5) & \text{otherwise.} \end{cases} \tag{48}$$

The solution is plotted at $t = 64$ μs (weak impact) and $t = 41$ μs (strong impact) in Figs. 8 and 9. Solution with the Lie implementation agrees with the analytical solution assuming constant ρG for the weak impact since density variations are small. For the strong impact, noticeable differences are observed: the analytical solution assuming constant ρG underpredicts pressure and the (negative) normal stress, $p - \tau_{11}^{(e)}$, results and overpredicts density between the shocks, compared to the numerical solutions. Again, the discrepancy is due to the invalidity of the constant ρG assumption necessary to obtain the analytical solution. The spike at the origin, also observed in [25], is attributed to overheating [59,11]; fixes have been proposed to address this issue [23]. For both impact velocities, the effect of the objective stress rates is negligible since the y-velocity is zero. Similar results are obtained at higher resolutions.
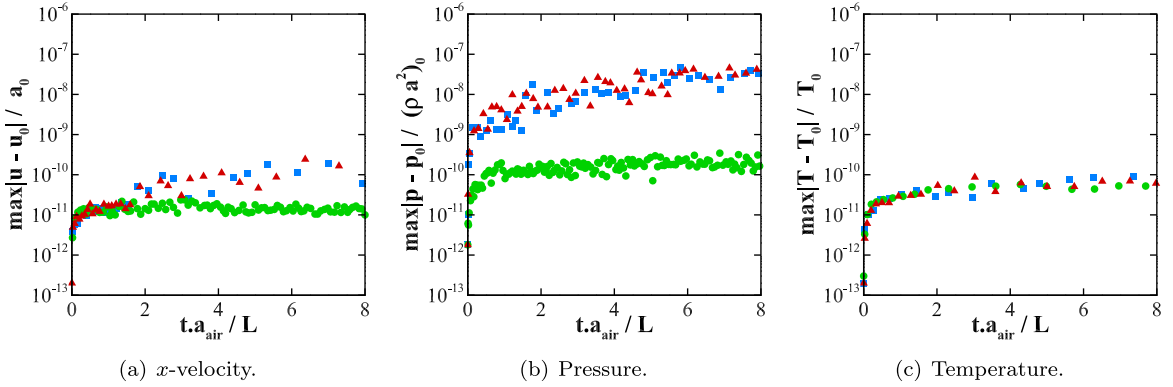
(a) x-velocity. (b) Pressure. (c) Temperature.

Fig. 5. Time histories of normalized L_∞ errors for the interface advection problem through two periods. Blue squares: Newtonian medium; red triangles: viscoelastic medium ($\mu_b = \mu_s = 5$ mPa s, $G = 1$ MPa); green circles: viscoelastic medium ($\mu_b = \mu_s = 5$ mPa s, $G = 1$ GPa).
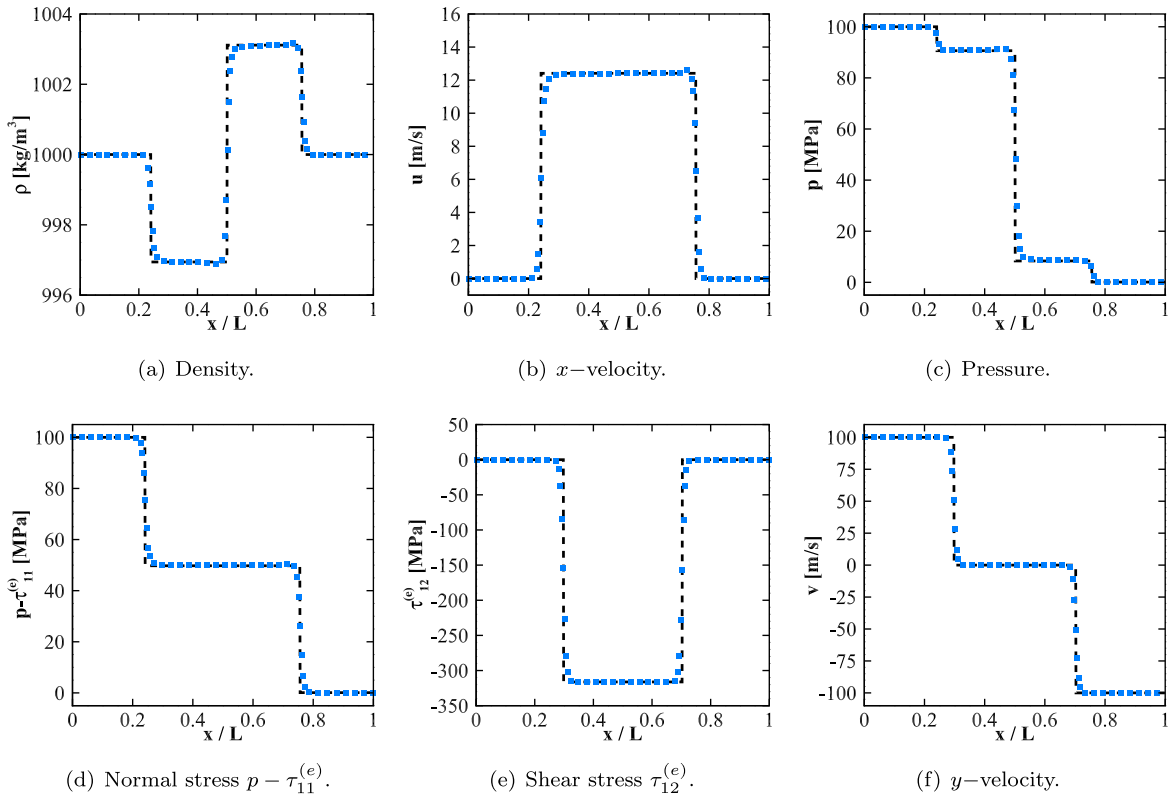

(a) Density. (b) x−velocity. (c) Pressure.

(d) Normal stress $p - \tau_{11}^{(e)}$. (e) Shear stress $\tau_{12}^{(e)}$. (f) y−velocity.

Fig. 6. Shock tube problem in an elastic medium for pressure ratio 1000 : 1 at $t = 64$ μs for the Lie derivative implementation (blue squares) along with the analytical solution (black dotted line).

Expansion-wave problem. We consider weak ($U = 50$ m/s) and strong ($U = 800$ m/s) expansions, with initial conditions

$$(\rho, u, v, p) = \begin{cases} (1000, -U, 0, 10^5) & \text{if} \quad x/L \in [0, 0.5], \\ (1000, U, 0, 10^5) & \text{otherwise.} \end{cases} \tag{49}$$

The solution is plotted at $t = 64$ μs (weak expansion) and $t = 40$ μs (strong expansion) in Figs. 10 and 11. Here again, the numerical solution with Lie derivative implementation agree with the analytical solution for the weak expansion since density variations are small; overheating is discernible in the pressure at the origin. For the strong expansion, noticeable differences are observed: the analytical solution with constant ρG overpredicts both pressure and density. The effect of the objective stress rate is negligible since the y-velocity is zero. Again, the discrepancy is due to the invalidity of the constant ρG assumption necessary to compute the analytical solution.

(a) Density.

(b) $x-$velocity.

(c) Pressure.

(d) Elastic stress $\tau_{11}^{(e)}$.
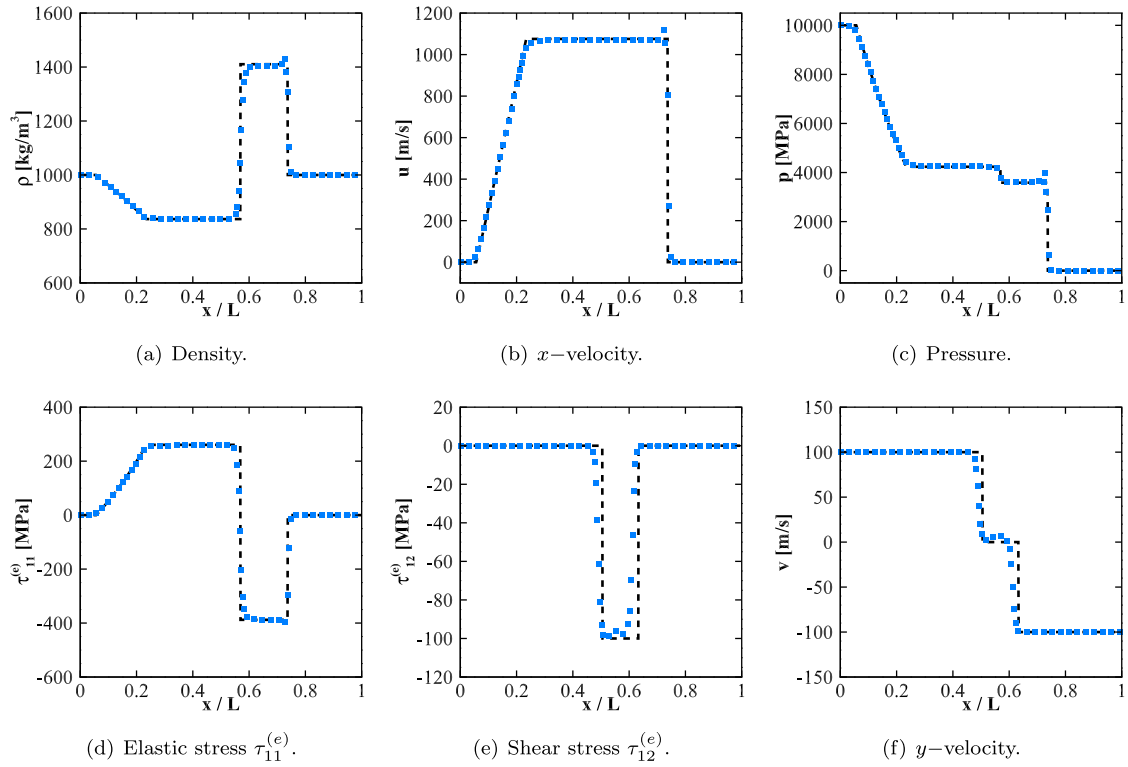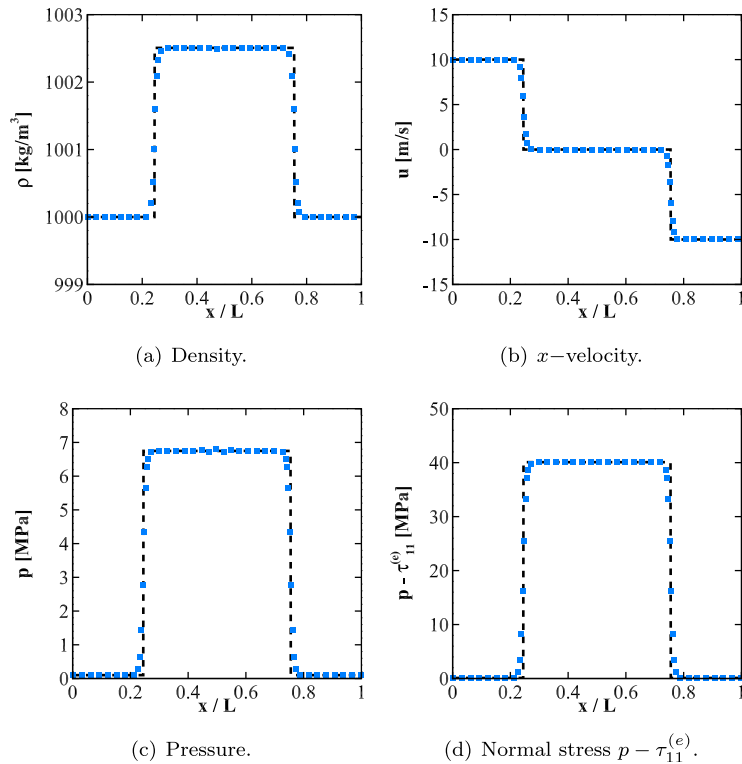
(e) Shear stress $\tau_{12}^{(e)}$.

(f) $y-$velocity.

Fig. 7. Shock tube problem in an elastic medium with pressure ratio $10^5 : 1$ at $t = 64$ μs for the Lie derivative implementation (blue squares) along with the analytical solution (black dotted line).

(a) Density.

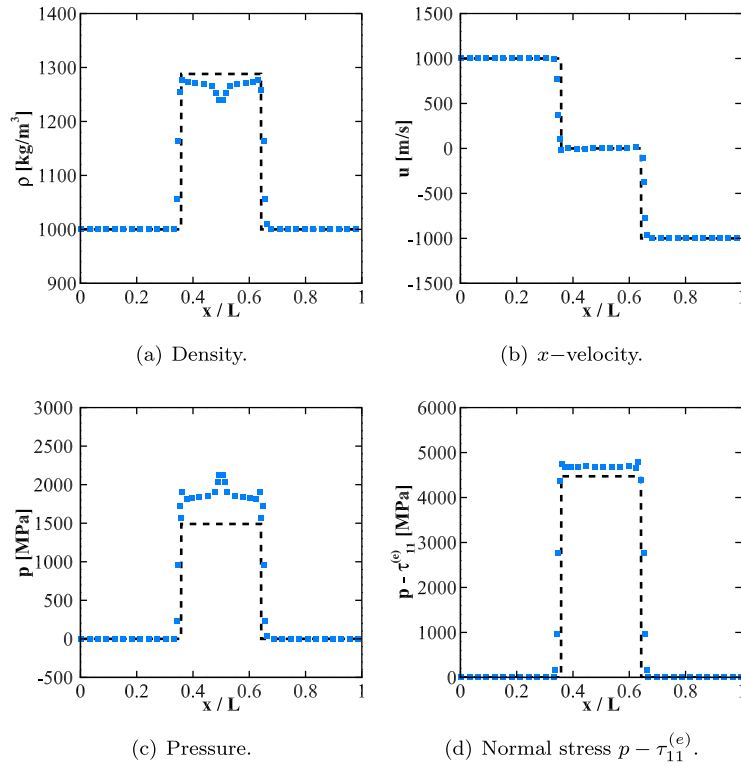(b) $x-$velocity.

(c) Pressure.

(d) Normal stress $p - \tau_{11}^{(e)}$.

Fig. 8. Weak impact problem (20 m/s velocity difference) in an elastic medium at $t = 64$ μs for the Lie derivative implementation (blue squares) along with analytical solution (black dotted line).

Fig. 9. Strong impact problem (2000 m/s velocity difference) in an elastic medium at $t = 41$ μs for the Lie derivative implementation (blue squares) along with the analytical solution (black dotted line).

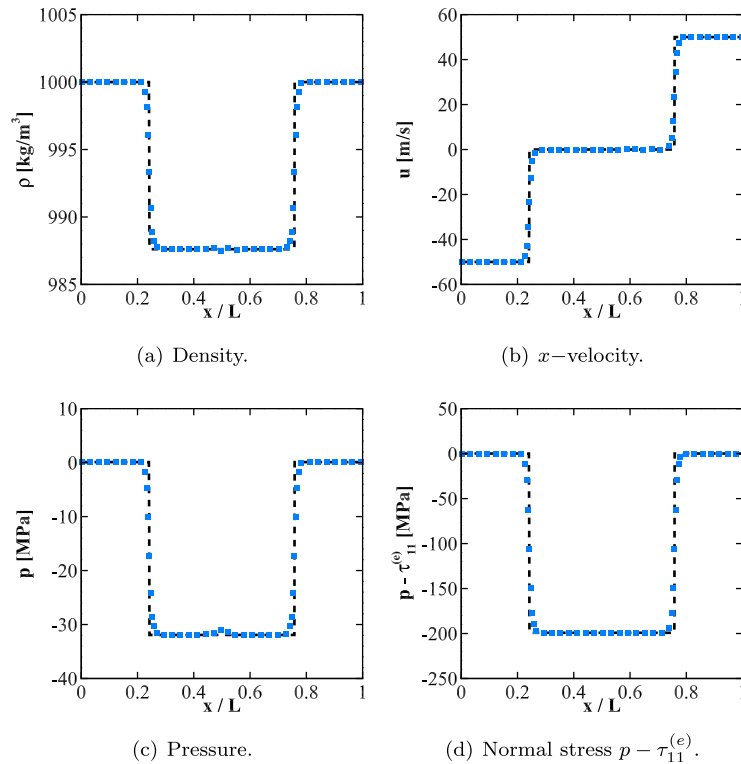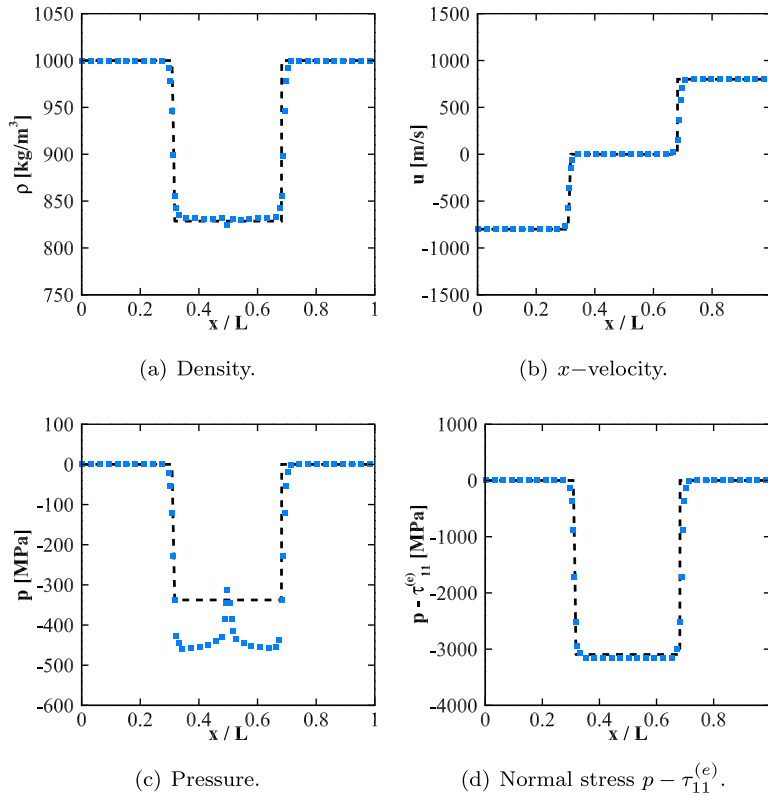**Fig. 10.** Weak expansion problem (100 m/s velocity difference) in an elastic medium at $t = 64$ μs for the Lie derivative implementation (blue squares) along with the analytical solution (black dotted line).

(a) Density.

(b) x−velocity.

(c) Pressure.

(d) Normal stress $p - \tau_{11}^{(e)}$.

Fig. 11. Strong expansion problem (1600 m/s velocity difference) in an elastic medium at $t = 40$ μs for the Lie derivative implementation (blue squares) along with the analytical solution (black dotted line).

5.4. Multi-material Riemann problem

To verify the extension of the five-equations multiphase model to viscoelastic media with shocks, we extend the multi-material Riemann problem in [2,56,3] to include viscoelasticity,

$$(\rho, u, v, p, \alpha^{(1)}) = \begin{cases} (1000, 0, 0, 10^9, 1) & \text{if } x/L \in [0, 0.7], \\ (50, 0, 0, 10^5, 0) & \text{otherwise.} \end{cases} \tag{50}$$

For comparison with the previous work, the right-hand side term in Eq. (34) is set to zero and the stiffened gas equation of state is used for the viscoelastic material and gas. The initial elastic stresses are $\tau_{11}^{(e)} = \tau_{22}^{(e)} = \tau_{12}^{(e)} = 0$. For the model viscoelastic material, $\kappa = 0.615$ W/(K m) and for the gas, $\kappa = 0.026$ W/(K m). The viscous ($\mu_b = \mu_s = 50$ mPa s) and Kelvin–Voigt ($\mu = 50$ mPa s and $G = 1$ GPa) solutions are plotted at $t = 240$ μs in Fig. 12, along with their respective analytical solutions. The analytical solutions were generated using the Riemann solver of [25], in which ρG is assumed constant. Our numerical results show good agreement with the analytical solution since the density ratio is large; all the relevant waves are captured, and no spurious oscillations are observed at any of the discontinuities for the Kelvin–Voigt solution. The solution with no elasticity exhibits an undershoot at the material interface, originating from the right-hand side term in Eq. (34) in the volume fraction equation, which can be addressed by implementing the equivalent six-equation multiphase model [70,61].

5.5. Shock wave-viscoelastic cylinder interaction

Inspired by [47], we consider the two-dimensional interaction of a shock in water with a viscoelastic cylinder to assess the capabilities to represent multi-dimensional wave propagation in viscoelastic media. The problem set-up is shown in Fig. 13; half of the domain is simulated given the symmetry. The domain extends three initial bubble radii in each direction from the bubble center: $x \in [-3$ mm, 3 mm$]$ and $y \in [0$ mm, 3 mm$]$. The initial cylinder radius is defined with a diffuse interface, similar to other multiphase studies [72], where the volume fraction is defined, $\alpha = \frac{1 - \tanh(\psi)}{2}$, where $\psi = (R - R_o)/\Delta x$, $R = \sqrt{x^2 + y^2}$ and $R_o = 1$ mm is the initial cylinder radius. Given the volume fraction and for constant velocity and pressure, the conservative variables ϕ are computed using the mixture relation, $\phi = \alpha \phi_1 + (1 - \alpha)\phi_2$.
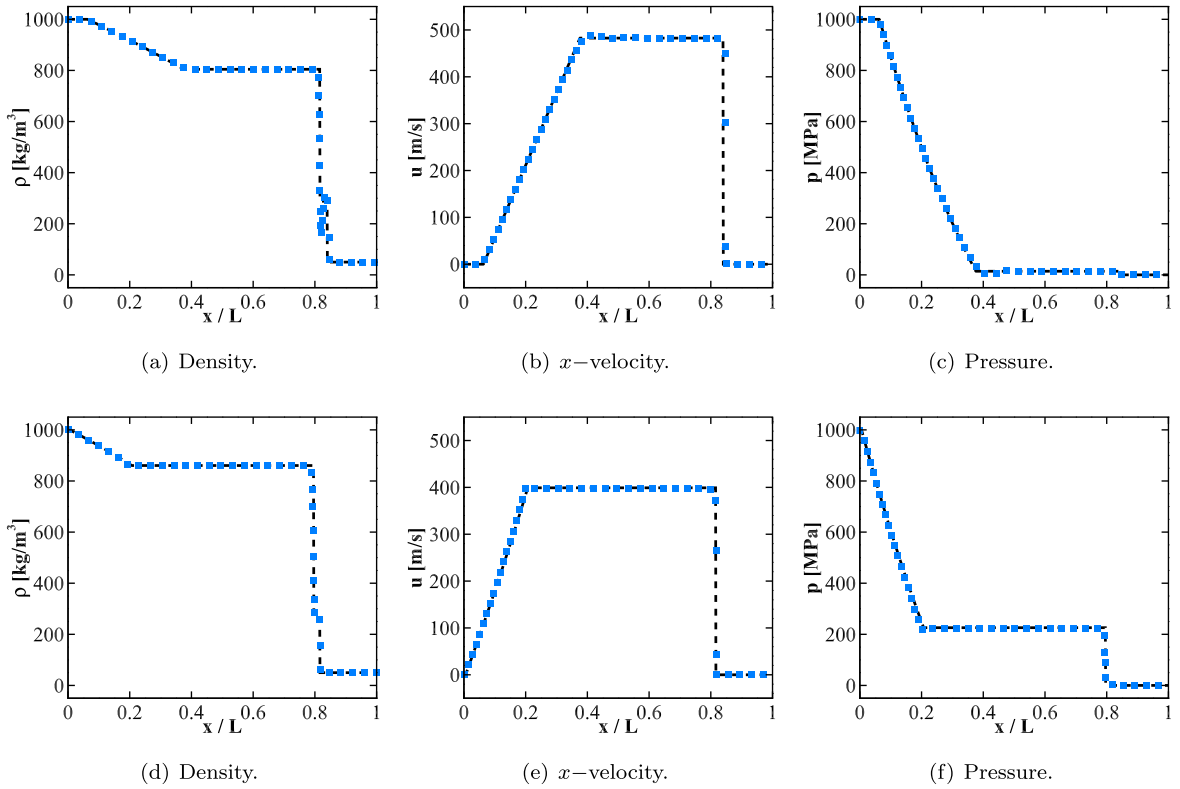
Fig. 12. Multi-material Riemann problem at $t = 240$ μs with analytical (black dashed line) and numerical (blue square) solutions for the viscous liquid-air shock wave (top row) and Kelvin–Voigt viscoelastic material-air shock wave (bottom row).
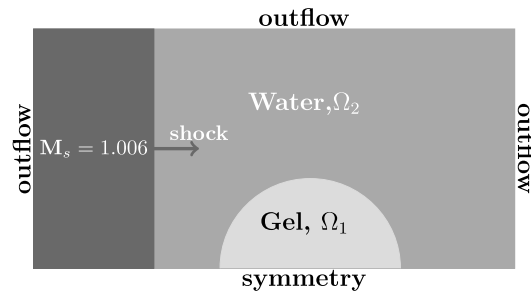

Fig. 13. Shock-viscoelastic cylinder interaction setup, analogous to the problem considered by Lombard and Piraux [47].

We use the generalized Zener model to represent the viscoelastic cylinder. The surrounding medium is water. For the viscoelastic cylinder, one relaxation time is considered with $\rho = 1000$ kg/m^3, $\mu_b = 50$ mPa s, $G = 1$ GPa, $G_r = 0.5$ GPa, $\varsigma^{(1)} = 1$, and $\theta^{(1)} = 15$ MHz. The remaining material properties for water and the model viscoelastic medium are in Table 1. The shear modulus values were selected to be two orders of magnitude higher than the incident shock wave pressure (i.e., $p = 10.1$ MPa) to highlight the effect of the elastic component of the stress inside the viscoelastic cylinder in the simulation. The shock wave is initialized at $x = -1.1 \times R_0$, using appropriate Rankine–Hugoniot conditions. The elastic contributions of the Cauchy stresses and the memory variables are initialized to zero. Four resolutions are considered: 32, 64, 128, 192, and 256 points per initial cylinder radius on a uniform mesh. Contours of the pressure and elastic component of the elastic stress tensor, $\tau_{12}^{(e)}$, are shown in Fig. 14, with 256 points per initial cylinder radius.

Upon interaction with the cylinder, the shock is partly reflected, partly transmitted, and diffracts around the cylinder (frame a). Due to the higher speed of sound in the viscoelastic material, the transmitted shock travels faster than the diffracting shock. As expected from one-dimensional results, the shear wave travels more slowly than the p-wave. As the transmitted shock reaches the distal side of the viscoelastic cylinder, it is partially transmitted and reflected back into the cylinder (frame b). The reflected internal rarefaction then interacts with the shear wave as the diffracted shock leaves the domain (frames c and d). The resulting transmitted shock propagates radially outward (frames d, e, and f). The trapped shock in the viscoelastic cylinder gives rise to a distorted shear wave structure with alternating concentrated regions of
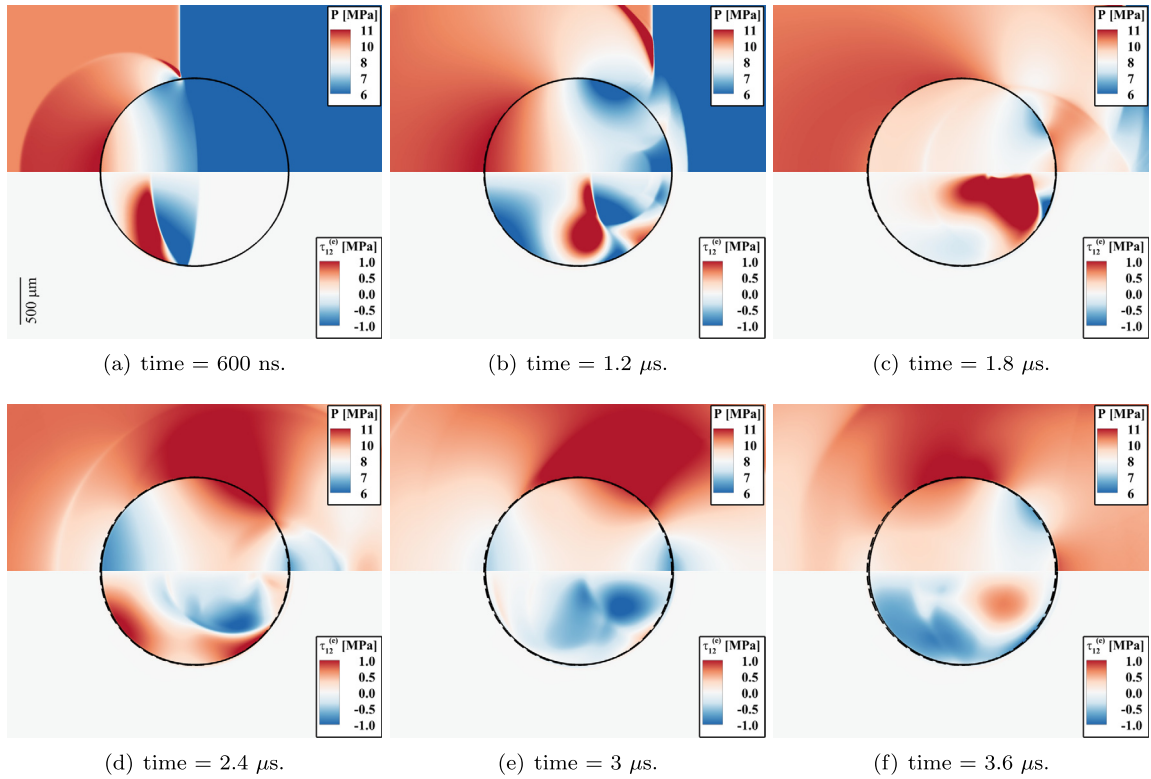
Fig. 14. Pressure (top) and elastic component of the stress tensor, $\tau_{12}^{(e)}$, (bottom) contours for the 2D interaction of a Mach 1.006 shock in water with a Zener-like viscoelastic medium with $G = 1$ GPa and $G_r = 0.5$ GPa. Dashed black: the initial cylinder location; solid black line: instantaneous interface location.
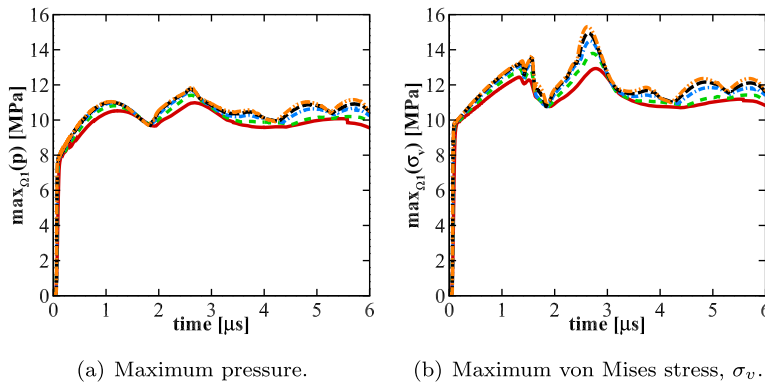

Fig. 15. Time evolution of quantities of interest in the 2D shock-viscoelastic cylinder interaction in the cylinder with 32 (solid red), 64 (green dash), 128 (blue dash–dot), 192 (black long dash), and 256 (orange dash–dot–dot) points per initial bubble radius.

negative and positive shear throughout the cylinder (frames d, e, and f). The shock wave minimally distorts the cylinder (in tension and shear).

The time evolution of two quantities of interest are the maximum pressure and elastic stress in the viscoelastic cylinder. For the elastic stress, we consider the von Mises stress,

$$\sigma_v = \sqrt{(\sigma_{11})^2 - \sigma_{11}\sigma_{22} + (\sigma_{22})^2 + 3(\sigma_{12})^2}, \tag{51}$$

which only incorporates the effects of pressure and all three components of the elastic stress. The time evolution of the maximum pressure and the von Mises stress is shown in Fig. 15 for the five spatial resolutions in the viscoelastic cylinder. The final time for the simulations is $t = 6$ μs when the incoming shock has left the domain, at which point the trapped shock waves in the viscoelastic cylinder have a negligible effect. The average maximum pressure experienced by the viscoelastic cylinder during the simulation is approximately 12 MPa, which is expected as most of the incoming shock wave is

transmitted into the cylinder since the acoustic impedance mismatch between the water and the viscoelastic gel is minimal. Using the von Mises stress, the maximum elastic strains, i.e., the von Mises strain, can be computed (applying Hooke's Law) and correspond to approximately 1.5% von Mises strain, thus justifying the small-strain approximation. The trapped transmitted shock (p-wave) is reflected back into the viscoelastic cylinder, generating the largest elastic stresses from $t = 2$ to 3 µs. The elastic stresses subsequently diminish substantially after the first internal reflection at $t = 3$ µs, as expected as the shock is transmitted mostly out of the cylinder; the remaining contributions are due to subsequent interactions with the slower shear wave. The pressure and stresses are not yet converged at the highest resolution presented here. Higher resolution would be needed to achieve convergence. Such interactions, where a shock, e.g., produced by a collapsing bubble, leads to p- and s-waves in the viscoelastic medium, are of interest when studying damage caused by the internal wave reflections in solids and the subject of future work.

6. Conclusions

We introduce a novel Eulerian approach for numerical simulations of wave propagation in heterogeneous viscoelastic media, with application to compressible materials described by linear constitutive relations, specifically Maxwell, Kelvin–Voigt or generalized Zener models. We extend the five-equations multiphase interface-capturing model, based on the idea that all the materials (gases, liquids, solids) obey the same equation of state with spatially varying properties, to incorporate the constitutive relation; interfaces are thus represented by discontinuities in material properties. To represent strains in an Eulerian framework, we utilize a hypoelastic model and implement the Lie objective derivative of the constitutive relations to evolve the strain rates instead of strains. As a result, additional evolution equations must be solved for the components of the elastic stress tensor and stress relaxation terms. Our numerical framework is explicit in time and space, and high-order accurate. The spatial scheme is based on a solution-adaptive approach, where central differences are used in smooth regions and high-order shock capturing at discontinuities (material interfaces, contacts and shocks). The method is verified using a stringent suite of test problems involving smooth wave, shock, shear and contact waves problems in viscoelastic media. At least fourth-order accuracy is achieved in smooth problems, and the correct wave speeds are obtained. Eigenanalysis confirms that our Lie derivative implementation yields correct results. Spurious pressure and temperature errors at interfaces are shown to be prevented, and all wave families are accurately represented. We consider a two-dimensional problem to further demonstrate the robustness of the method (shock-viscoelastic solid interaction). Overall, this work advances our capabilities to compute fully coupled fluid–solid problems. Further investigations into the inclusion of more complex constitutive relations, particularly those involving finite deformations, will be pursued in the future.

Acknowledgements

References

[1] R. Abgrall, How to prevent pressure oscillations in multicomponent flow calculations: a quasi conservative approach, J. Comput. Phys. 125 (1996) 150–160.

[2] S. Alahyari Beig, E. Johnsen, Maintaining interface equilibrium conditions in compressible multiphase flows using interface capturing, J. Comput. Phys. 302 (2015) 548–566.

[3] G. Allaire, S. Clerc, S. Kokh, A five-equation model for the simulation of interfaces between compressible fluids, J. Comput. Phys. 181 (2002) 577–616.

[4] G. Altmeyer, B. Panicaud, E. Rouhaud, M. Wang, A. Roos, R. Kerner, Viscoelasticity behavior for finite deformations, using a consistent hypoelastic model based on Rivlin materials, Contin. Mech. Thermodyn. 28 (6) (2016) 1741–1758.

[5] G. Altmeyer, E. Rouhaud, B. Panicaud, A. Roos, R. Kerner, M. Wang, Viscoelastic models with consistent hypoelasticity for fluids undergoing finite deformations, Mech. Time-Depend. Mater. 19 (2015) 375–395.

[6] M. Arienti, P. Hung, E. Morano, J.E. Shepherd, A level set approach to Eulerian–Lagrangian coupling, J. Comput. Phys. 185 (2003) 213–251.

[7] M. Baer, J. Nunziato, A two-phase mixture theory for the deflagration-to-detonation transition (ddt) in reactive granular materials, Int. J. Multiph. Flow 12 (1986) 861–889.

[8] Y.A. Bahei-El-Din, G.J. Dvorak, O.J. Fredricksen, A blast-tolerant sandwich plate design with a polyurea interlayer, Int. J. Solids Struct. 43 (2006) 7644–7658.

[9] P.T. Barton, R. Deiterding, D. Meiron, D. Pullin, Eulerian adaptive finite-difference method for high-velocity impact and penetration problems, J. Comput. Phys. 240 (2013) 76–99.

[10] P.T. Barton, D. Drikakis, An Eulerian method for multi-component problems in non-linear elasticity with sliding interfaces, J. Comput. Phys. 229 (2010) 5518–5540.

[11] P.T. Barton, D. Drikakis, E. Romenski, V.A. Titarev, Exact and approximate solutions of Riemann problems in non-linear elasticity, J. Comput. Phys. 228 (2009) 7046–7068.

[12] P.T. Barton, B. Obadia, D. Drikakis, A conservative level-set based method for compressible solid/fluid problems on fixed grids, J. Comput. Phys. 230 (2011) 7867–7890.

[13] E. Bécache, A. Ezziani, P. Joly, A mixed finite element approach for viscoelastic wave propagation, Comput. Geosci. 8 (2005) 255–299.

[14] J.M. Carcione, Seismic modeling in viscoelastic media, Geophysics 58 (1993) 110–120.

[15] J.M. Carcione, Wave Fields in Real Media: Wave Propagation in Anisotropic, Anelastic, Porous and Electromagnetic Media, 3rd edition, Elsevier Science, 2014.

[16] V. Coralic, T. Colonius, Finite-volume WENO scheme for viscous compressible multicomponent flows, J. Comput. Phys. 274 (2014) 95–121.

[17] A. de Brauer, A. Iollo, T. Milcent, A Cartesian scheme for compressible multimaterial models in 3D, J. Comput. Phys. 313 (2016) 121–143.

[18] B. Despres, A geometrical approach to nonconservative shocks and elastoplastic shocks, Arch. Ration. Mech. Anal. 186 (2007) 275–308.

[19] M. Dumbser, I. Peshkov, E. Romenski, O. Zanotti, High order ADER schemes for a unified first order hyperbolic formulation of continuum mechanics: viscous heat-conducting fluids and elastic solids, J. Comput. Phys. 314 (2015) 824–862.

[20] A.C. Eringen, Nonlinear Theory of Continuous Media, McGraw–Hill, New York, NY, 1962.

[21] N. Favrie, S. Gavrilyuk, Mathematical and numerical model for nonlinear viscoplasticity, Philos. Trans. R. Soc. A, Math. Phys. Eng. Sci. 369 (2011) 2864–2880.

[22] N. Favrie, S.L. Gavrilyuk, R. Saurel, Solid–fluid diffuse interface model in cases of extreme deformations, J. Comput. Phys. 228 (2009) 6037–6077.

[23] R.P. Fedkiw, A. Marquina, B. Merriman, An isobaric fix for the overheating problem in multimaterial compressible flows, J. Comput. Phys. 148 (1999) 545–578.

[24] Y.-C. Fung, Biomechanics, Springer New York, New York, NY, 1993.

[25] S.L. Gavrilyuk, N. Favrie, R. Saurel, Modelling wave dynamics of compressible elastic materials, J. Comput. Phys. 227 (2008) 2941–2969.

[26] S.K. Godunov, E.I. Romenskii, Nonstationary equations of nonlinear elasticity theory in Eulerian coordinates, J. Appl. Mech. Tech. Phys. 13 (1972) 868–884.

[27] S.K. Godunov, E.I. Romenskii, Elements of Continuum Mechanics and Conservation Laws, Springer US, Boston, MA, 2003.

[28] Y. Gorsse, A. Iollo, T. Milcent, H. Telib, A simple Cartesian scheme for compressible multimaterials, J. Comput. Phys. 272 (2014) 772–798.

[29] J.T. Grétarsson, R. Fedkiw, Fully conservative leak-proof treatment of thin solid structures immersed in compressible fluids, J. Comput. Phys. 245 (2013) 160–204.

[30] F.H. Harlow, A.A. Amsden, Fluid Dynamics, Los Alamos Scientific Laboratory, Los Alamos, NM, 1971.

[31] A. Harten, P.D. Lax, B. van Leer, On upstream differencing and Godunov-type schemes for hyperbolic conservation laws, SIAM Rev. 25 (1983) 35–61.

[32] M.T. Henry de Frahan, S. Varadan, E. Johnsen, A new limiting procedure for discontinuous Galerkin methods applied to compressible multiphase flows with shocks and interfaces, J. Comput. Phys. 280 (2015) 489–509.

[33] G.-S. Jiang, C.-W. Shu, Efficient implementation of Weighted ENO schemes, J. Comput. Phys. 126 (1996) 202–228.

[34] E. Johnsen, On the treatment of contact discontinuities using WENO schemes, J. Comput. Phys. 230 (2011) 8665–8668.

[35] E. Johnsen, Analysis of numerical errors generated by slowly moving shock waves, AIAA J. 51 (2013) 1269–1274.

[36] E. Johnsen, T. Colonius, Implementation of WENO schemes in compressible multicomponent flow problems, J. Comput. Phys. 219 (2006) 715–732.

[37] A. Kapahi, S. Sambasivan, H.S. Udaykumar, A three-dimensional sharp interface Cartesian grid method for solving high speed multi-material impact, penetration and fragmentation problems, J. Comput. Phys. 241 (2013) 308–332.

[38] A. Kapahi, S. Sambasivan, H.S. Udaykumar, Simulation of collapse and fragmentation phenomena in a sharp interface Eulerian setting, Comput. Fluids 87 (2013) 26–40.

[39] A. Kapahi, H.S. Udaykumar, Dynamics of void collapse in shocked energetic materials: physics of void–void interactions, Shock Waves 23 (2013) 537–558.

[40] A. Kapahi, H.S. Udaykumar, Three-dimensional simulations of dynamics of void collapse in energetic materials, Shock Waves 23 (2013) 537–558.

[41] A.K. Kapila, R. Menikoff, J.B. Bdzil, S.F. Son, D.S. Stewart, Two-phase modeling of deflagration-to-detonation transition in granular materials: reduced equations, Phys. Fluids 13 (2001) 3002–3024.

[42] D. Klatt, U. Hamhaber, P. Asbach, J. Braun, I. Sack, Noninvasive assessment of the rheological behavior of human organs using multifrequency MR elastography: a study of brain and liver viscoelasticity, Phys. Med. Biol. 52 (2007) 7281–7294.

[43] A. Kulikovskii, N. Pogorelov, A. Semenov, K. Piechor, Mathematical Aspects of Numerical Solution of Hyperbolic Systems, Monographs and Surveys in Pure and Applied Mathematics, vol. 118, CRC Press, 2000.

[44] P. Le Floch, F. Olsson, A second-order Godunov method for the conservation laws of nonlinear elastodynamics, Impact Comput. Sci. Eng. 2 (1990) 318–354.

[45] O. Le Métayer, J. Massoni, R. Saurel, Modelling evaporation fronts with reactive Riemann solvers, J. Comput. Phys. 205 (2005) 567–610.

[46] O. Le Métayer, R. Saurel, The Noble–Abel Stiffened-Gas equation of state, Phys. Fluids 28 (2016) 1–22.

[47] B. Lombard, J. Piraux, Numerical treatment of two-dimensional interfaces for acoustic and elastic waves, J. Comput. Phys. 195 (2004) 90–116.

[48] B. Lombard, J. Piraux, Numerical modeling of transient two-dimensional viscoelastic waves, J. Comput. Phys. 230 (2011) 6099–6114.

[49] A. López Ortega, M. Lombardini, D.J. Hill, Converging shocks in elastic–plastic solids, Phys. Rev. E 84 (2011) 1–21.

[50] A. López Ortega, M. Lombardini, D. Pullin, D. Meiron, Numerical simulation of elastic–plastic solid mechanics using an Eulerian stretch tensor approach and HLLD Riemann solver, J. Comput. Phys. 257 (2014) 414–441.

[51] J. Massoni, R. Saurel, B. Nkonga, R. Abgrall, Proposition de méthodes et modèles eulériens pour les problèmes à interfaces entre fluides compressibles en présence de transfert de chaleur, Int. J. Heat Mass Transf. 45 (2002) 1287–1307.

[52] G. Miller, P. Colella, A conservative three-dimensional Eulerian method for coupled solid–fluid shock capturing, J. Comput. Phys. 183 (2002) 26–82.

[53] G.H. Miller, An iterative Riemann solver for systems of hyperbolic conservation laws, with application to hyperelastic solid mechanics, J. Comput. Phys. 193 (2004) 198–225.

[54] G.H. Miller, P. Colella, A high-order Eulerian Godunov method for elastic–plastic flow in solids, J. Comput. Phys. 167 (2001) 131–176.

[55] A. Morro, A thermodynamic approach to rate equations in continuum physics, J. Phys. Sci. Appl. 7 (6) (2017) 15–23.

[56] A. Murrone, H. Guillard, A five equation reduced model for compressible two phase flow problems, J. Comput. Phys. 202 (2005) 664–698.

[57] S. Ndanou, N. Favrie, S. Gavrilyuk, Criterion of hyperbolicity in hyperelasticity in the case of the stored energy in separable form, J. Elast. 115 (2013) 1–25.

[58] S. Ndanou, N. Favrie, S. Gavrilyuk, Multi-solid and multi-fluid diffuse interface model: applications to dynamic fracture and fragmentation, J. Comput. Phys. 295 (2015) 523–555.

[59] W. Noh, Errors for calculations of strong shocks using an artificial viscosity and an artificial heat flux, J. Comput. Phys. 72 (1987) 78–120.

[60] J. Palacio-Torralba, S. Hammer, D.W. Good, S. Alan McNeill, G.D. Stewart, R.L. Reuben, Y. Chen, Quantitative diagnostics of soft tissue through viscoelastic characterization using time-based instrumented palpation, J. Mech. Behav. Biomed. Mater. 41 (2015) 149–160.

[61] M. Pelanti, K.M. Shyue, A mixture-energy-consistent six-equation two-phase numerical model for fluids with interfaces, cavitation and evaporation waves, J. Comput. Phys. 259 (2014) 331–357.

[62] G. Perigaud, R. Saurel, A compressible flow model with capillary effects, J. Comput. Phys. 209 (2005) 139–178.

[63] B.J. Plohr, D.H. Sharp, A conservative Eulerian formulation of the equations for elastic flow, Adv. Appl. Math. 9 (1988) 481–499.

[64] O. Rijensky, D. Rittel, Polyurea coated aluminum plates under hydrodynamic loading: does side matter?, Int. J. Impact Eng. 98 (2016) 1–12.

[65] J.O.A. Robertsson, J.O. Blanch, W.W. Symes, Viscoelastic finite-difference modeling, Geophysics 59 (1994) 1444–1456.

[66] S.K. Sambasivan, H.S. UdayKumar, Ghost fluid method for strong shock interactions Part 2: immersed solid boundaries, AIAA J. 47 (2009) 2923–2937.

[67] R. Saurel, R. Abgrall, A multiphase Godunov method for compressible multifluid and multiphase flows, J. Comput. Phys. 150 (1999) 425–467.

[68] R. Saurel, R. Abgrall, A simple method for compressible multifluid flows, SIAM J. Sci. Comput. 21 (1999) 1115–1145.

[69] R. Saurel, O. Lemetayer, A multiphase model for compressible flows with interfaces, shocks, detonation waves and cavitation, J. Fluid Mech. 431 (2001) 239–271.

[70] R. Saurel, F. Petitpas, R.A. Berry, Simple and efficient relaxation methods for interfaces separating compressible fluids, cavitating flows and shocks in multiphase mixtures, J. Comput. Phys. 228 (2009) 1678–1712.

[71] S. Schoch, K. Nordin-Bates, N. Nikiforakis, An Eulerian algorithm for coupled simulations of elastoplastic-solids and condensed-phase explosives, J. Comput. Phys. 252 (2013) 163–194.
[72] R.K. Shukla, C. Pantano, J.B. Freund, An interface capturing method for the simulation of multi-phase compressible flows, J. Comput. Phys. 229 (2010) 7411–7439.
[73] K.-M. Shyue, An efficient shock-capturing algorithm for compressible multicomponent problems, J. Comput. Phys. 142 (1998) 208–242.
[74] K.S. Surana, Y. Ma, A. Romkes, J.N. Reddy, The rate constitutive equations and their validity for progressively increasing deformation, Mech. Adv. Mat. Struct. 17 (7) (2010) 509–533.
[75] V.A. Titarev, E.F. Toro, ADER: arbitrary high order Godunov approach, J. Sci. Comput. 17 (1–4) (2002) 609–618.
[76] A. Tiwari, J.B. Freund, C. Pantano, A diffuse interface model with immiscibility preservation, J. Comput. Phys. 252 (2013) 290–309.
[77] L. Tran, H. Udaykumar, A particle-level set-based sharp interface Cartesian grid method for impact, penetration, and void collapse, J. Comput. Phys. 193 (2004) 469–510.
[78] L. Tran, H.S. Udaykumar, Simulation of void collapse in an energetic material, Part 2: reactive case, J. Propuls. Power 22 (2006) 959–974.
[79] L. Tran, H.S. Udaykumar, Simulation of void collapse in an energetic material, Part I: inert case, J. Propuls. Power 22 (2006) 947–958.
[80] J.A. Trangenstein, P. Colella, A higher-order Godunov method for modeling finite deformation in elastic–plastic solids, Commun. Pure Appl. Math. 44 (1991) 41–100.
[81] H.S. Udaykumar, L. Tran, D.M. Belk, K.J. Vanden, An Eulerian method for computation of multimaterial impact with ENO shock-capturing and sharp interfaces, J. Comput. Phys. 186 (2003) 136–177.
[82] P. Ván, A. Berezovski, C. Papenfuss, Thermodynamic approach to generalized continua, Contin. Mech. Thermodyn. 26 (2014) 403–420.
[83] E. Vlaisavljevich, K.-W. Lin, M.T. Warnez, R. Singh, L. Mancia, A.J. Putnam, E. Johnsen, C. Cain, Z. Xu, Effects of tissue stiffness, ultrasound frequency, and pressure on histotripsy-induced cavitation bubble behavior, Phys. Med. Biol. 60 (2015) 2271–2292.
[84] A.S. Wineman, Mechanical Response of Polymers: An Introduction, Cambridge University Press, 2000.
[85] Y.L. Young, Z. Liu, W. Xie, Fluid-structure and shock-bubble interaction effects during underwater explosions near composite structures, J. Appl. Mech. 76 (2009) 1–10.
[86] C. Zener, Mechanical behavior of high damping metals, J. Appl. Phys. 18 (1947) 1022–1025.